Advanced electrode materials for nonaqueous calcium rechargeable batteries

Chunhong Chen,[a] Fangyi Shi,[a,b] Zheng-Long Xu[a,c*]

[a] Department of Industrial and Systems Engineering, the Hong Kong Polytechnic University, Hung Hom, Hong Kong

[b] Department of Applied Physics, The Hong Kong Polytechnic University, Hung Hom, Hong Kong

[c] State Key Laboratory of Ultra-precision Machining Technology, The Hong Kong Polytechnic University, Hung Hom, Hong Kong

*Corresponding author: ZL Xu zhenglong.xu@polyu.edu.hk

Abstract

Calcium (Ca)-based rechargeable batteries (CRBs) have been considered one of the most promising post lithium ion battery technologies because of the natural abundance of Ca, high volumetric capacity compared to monovalent metal batteries, and the low reduction potential of Ca^{2+}/Ca. Recently, a breakthrough of Ca reversible plating and stripping at the Ca metal anode in carbonate electrolytes evokes the study of Ca rechargeable batteries. This critical review presents the state-of-the-art progress made in exploring potential electrode materials including Ca metal anode, alternative graphite and alloy-typed anodes, cathode materials undergoing interaction or conversion reactions. Suitable electrolytes are also required to ensure compatibility of each cell components, which is essential toward high-performance Ca full battery. The performance assessment and mechanism analysis are further discussed to evaluate the current progress and existing challenges regarding the performance promises and insufficient understandings for the Ca battery technology. To conclude, this review provides a comprehensive understanding of the underlying mechanisms and challenges that need to be addressed to promote commercialization of CRBs.

1. Introduction

The ever-increasing energy demand, limited fossil fuel reserves, and increasing environmental concerns have made the development of sustainable energy crucial. The intermittent nature of renewable energy sources, such as wind and solar power, lead to an inconsistent power supply, necessitating energy storage. Rechargeable batteries based on electrochemical reactions provide promising solutions with their high energy conversion efficiency, high flexibility, and wide affordability.[1,2] Since the early 1990s, lithium ion batteries (LIBs) have become the most common choice to power portable electric devices. However, emerging applications such as electric vehicles and smart grids require new battery technologies with higher energy densities, lower cost, and better safety than current LIBs.[3–6] Additionally, the unevenly distributed lithium resources in the Earth's crust (22 ppm) raise concerns for large-scale supply in the future. While the long-term availability of lithium resources remains debatable,[6] the recent leap in the price of lithium carbonate, *i.e.*, the main precursor for lithium, clearly indicates the need to explore post-LIB technologies.[7]

Multivalent rechargeable batteries have been considered promising candidates because, in principle, multivalent ion insertion/extraction is associated with multiple electron transfer,[8] potentially leading to higher energy densities than the monovalent ion can carry.[9] In addition, non-toxic multivalent elements are much more abundant in the Earth's crust (41,500 ppm for Ca, 27,640 ppm for Mg, 83,000 ppm for Al),[8] implying lower material costs. Some multivalent metal (*i.e.*, Mg and Al) anodes also show dendrite-free plating behaviors, indicating ideal metal anodes for high-energy and safe energy storage devices.[10–12] Ca rechargeable batteries (CRBs), especially those based on nonaqueous electrolytes, have several advantages over Mg or Al-based chemistries: (i) the reduction potential of Ca/Ca^{2+} (-2.9 V vs. standard hydrogen electrode (SHE)) is close to that of lithium (-3.04 V vs. SHE for Li/Li^{+}) and much lower than that of other multivalent cations (-0.76 V vs. SHE for Zn/Zn^{2+}, -2.4 V vs. for Mg/Mg^{2+}, and -

1.7 V vs. SHE for Al/Al^{3+}), indicating potentially high voltages and energy densities for CRBs;[12] (ii) Polarization strength ($P = q*r^2$, where q is the charge number of the cation and r is the ion radius) of Ca^{2+}(1.92×10^4 pm^{-2}), is smaller than that for Mg^{2+} (4.73×10^4 pm^{-2}) and Al^{3+} (5.66×10^4 pm^{-2}),[13,14] which allows faster cation diffusion kinetics; (iii) different from the inevitable dendrite formation in Li metal batteries, the Ca metal anodes are regarded as dendrite-free during cycling, indicating safe Ca metal batteries.[15–17]

The configuration and working principle for CRBs resemble these of LIBs, where the charge carrier Ca^{2+} shuttles forth and back between the anode and the cathode during releasing and storing the electrochemical energies. However, progress in developing CRBs faces some fundamental challenges; for instance, the Ca metal anode is irreversible in polar aprotic electrolytes due to the formation of Ca^{2+} blocking films on Ca metal during the first discharge; thus, compatible electrolytes are needed.[18] This issue engenders the difficulties to choose compatible anode materials and electrolytes. Additionally, it is also challenging to quest suitable cathode materials with high voltage, high-rate capability and large Ca storage capacities.[19,20] The relatively large ionic size and divalent nature of Ca^{2+}, compared to the extensively investigated monovalent ion systems (*i.e.*, Li^+ and Na^+), tend to make the intercalation kinetics in diffusion channels of cathodes sluggish. Moreover, Ca^{2+} with large ionic size intercalated in the host is predicted to cause large volume changes (*i.e.*, 25% for Ca_xTiSe_2,[21] 68-90% for β-MoO_2,[22] 25% for spinel $CaMn_2O_4$,[23] and 20% for perovskite $CaMO_3$,[24] M = Cr, Mn, Fe, Co and Ni), which triggers a premature structural degradation of the cathode structure. Therefore, exploring advanced electrodes is the key to achieving practical CRBs.

This review presents the recent accomplishments and challenges for CRBs. For anode materials, the correlations among the plating/stripping behaviors of Ca metal, electrolyte formulations, and electrochemical performance, have been presented. Non-Ca metal anodes,

such as graphite and Sn, are also discussed. For cathode materials, intercalation process in materials like van der Waals layered compounds, transition metal oxides, Prussian blue, and polyanion compounds, and conversion reactions in materials based on sulfur, oxygen and organic materials have been covered. Finally, studies reporting performance and fundamental findings are provided in context to give fresh perspectives for the future development of CRBs.

2. Anode materials

2.1 Calcium metal anode

Ca metal has been considered as the most attractive anode material for CRBs due to its lowest working potential, high volumetric capacity of 2073 Ah L^{-1} and high specific capacity of 1337 mAh g^{-1}.[15] However, efficient plating and stripping of Ca metal at room temperature has not been achieved until recently. An early attempt was conducted by Staniewics *et al.*[25] studying the electrochemical behaviors of Ca-SO_2Cl_2 system, which failed to produce any plating Ca because of the formation of ionic insulating $CaCl_2$ passivation layer on Ca metal. To estimate whether the established aprotic electrolytes in LIBs were suitable to Ca metal anode, Aurbach *et al.*[18] extensively cycled Ca in a few organic electrolytes using acetonitrile (AN), tetrahydrofuran (THF), γ-butyrolactone and propylene carbonate (PC) solvents with $Ca(ClO_4)_2$, $Ca(BF_4)_2$, $TBABF_4$ and $LiClO_4$ salts. Cyclic voltammetry (CV) analyses (Fig. 1a) exhibited high current densities of approximately 3 mA cm^{-2} for Ca stripping but the Ca deposition current was negligible (< 0.5 mA cm^{-2}) in all electrolytes. Structural characterizations presented ionic insulating phases (*i.e.*, $Ca(OH)_2$, $CaCO_3$, $CaCl_2$, alkoxide, ester and carboxylates) on Ca metal surface (Fig. 1b). The ionic insulating film was believed to prevent Ca deposition (Fig. 1c). Henceforth, the Ca metal battery study was stalled, especially after the successful triumph of commercial LIBs in 1990s.

In 2016, Ponrouch *et al.*[26] reported the first reversible Ca plating-stripping in a 0.45 M $Ca(BF_4)_2$ ethylene carbonate/propylene carbonate (EC/PC) electrolyte at elevated temperatures

(75-100 ℃). Apparent redox peaks for Ca plating on stainless steel appeared in CV curves and maintained over 30 cycles at 100 ℃ (Fig. 2a). The reversible Ca metal anode was found to be salt-, concentration- and temperature-dependent, where less activity towards Ca deposition was observed in $Ca(ClO_4)_2$ and $Ca(TFSI)_2$-based electrolytes, a low concentration electrolyte (0.3 M $Ca(BF_4)_2$ EC/PC) or at low operating temperatures. The harsh working conditions, especially the high cycling temperatures, make this pioneering work unacceptable for practical application. To figure out whether the high temperature is indispensable to Ca deposition, Biria *et al.*[27] cycled a three-electrode cell (Cu as the working electrode, Ca as the reference electrode and Pt as counter electrode) in 1 M $Ca(BF_4)_2$ EC/PC electrolyte at room temperature (Fig. 2b). Interestingly, Ca was reversibly deposited and removed over 10 cycles with coulombic efficiencies (CEs) up to 95 %. It was tentatively explained that the Cu substrate and room temperature conditions suppressed the growth of CaF_2 film (Fig. 2c).

Another pioneering work for reversible Ca metal anode was conducted by Want *et al.*,[28] who found Ca was able to plate in 1 M $Ca(BH_4)_2$ THF electrolyte at a current density of 1 mA cm^{-2} with a low polarization potential of ~100 mV in excess of 50 cycles at room temperature (Fig. 2d) while no electrochemical response was observed in $Ca(TFSI)_2$ THF electrolyte, implying the paramount role of BH_4^- anion. The function of BH_4^- was investigated through linear sweep voltammetry measurements of Ca striping-plating on Pt or Au electrodes in $Ca(BH_4)_2$ THF electrolyte.[29] Scanning electron microscopy (SEM) images showed a smooth Ca deposition on Au electrode, in contrast, Pt surface was covered by discrete Ca islands (Fig. 2e). The difference was originated from the different BH_4^- dehydrogenation rates on Pt and Au substrates. The latter exhibited slower dehydrogenation to allow lateral diffusion of hydride prior to Ca^{2+} adsorption, leading to uniform Ca^{2+} reduction (Fig. 2e). Apart from BH_4^- anion, cation also plays an important role in regulating the Ca deposition. Jie *et al.*[30] reported that in a Ca||Au coin cell with 0.4 M $Ca(BH_4)_2$-0.4M $LiBH_4$ THF electrolyte, the initial CE was 84.4%,

which increased to 99.1% after 5 cycles and maintained at approximate 97.6% over 200 cycles (Fig. 2f-g). In contrast, the CEs of the cells cycling in $Ca(BH_4)_2$ THF electrolyte were about 80% in the first 10 cycles, and dropped to 60% after 20 cycles. The significantly improved cyclic stability in $Ca(BH_4)_2$-$LiBH_4$ electrolyte was attributable to the decreased coordination number of Ca^{2+} by Li^+ in the first solvation shell, suggesting the well-manipulated coordination structure of Ca^{2+} in electrolyte. Note that the THF-based electrolyte presents low anodic stability (~3V), which would limit the choice of high-voltage cathodes for CRBs.

In order to obtain a highly anodic stable electrolyte, a borate salt, calcium tetrakis (hexafluoroisopropyloxy) borate ($Ca[B(hfip)_4]_2$), was prepared[31,32] by reacting $Ca(BH_4)_2$ with hexafluoroisopropanol in DME, as shown in Fig. 3a.[31] Stripping and plating of Ca in 0.25 M $Ca[B(hfip)_4]_2$/DME electrolyte was demonstrated by CV tests in a three-electrode cell, showing low overpotentials for Ca deposition (at -0.3 V) and dissolution (at 0.22 V) (Fig. 3b). These values imply rapid kinetics and low desolvation energy for the borate electrolyte. Indeed, the $[B(hfip)_4]^-$ anion has been demonstrated effective for reversible Mg cycling in $Mg[B(hfip)_4]_2$ electrolyte.[33,34] Li *et al.*[31] calculated the average O-Ca bond length of DME-coordinated Ca^{2+} in $Ca[B(hfip)_4]_2$/DME to be 2.43 Å, which was longer than the 2.06 Å for O-Mg in the analogous Mg electrolyte, suggesting the lower desolvation energy of Ca^{2+} in the electrolyte. The cyclic stability of Ca metal in borate-based electrolyte was measured by cycling Ca//Ca symmetric cells at 0.2 mA cm^{-2} over 100 hours (Fig. 3c). The anodic stability of the $Ca[B(hfip)_4]_2$/DME electrolyte was measured to be 3.9 V, 4.2 V and 4.8 V for Pt, stainless steel and Al electrodes (Fig. 3d), respectively, which are much higher than that for $Ca(BH_4)_2$ THF as aforementioned.

To optimize the cyclability of Ca metal anode in $Ca[B(hfip)_4]_2$-based electrolytes, parameters in terms of the electrolyte concentration, types of ether solvents, and working electrodes were controlled. Shyamsunder *et al.*[32] found that the Ca was able to cycle with a

high current density of 0.5 mA cm^{-2}, a low polarization of 0.17 V and high CEs of 92-95% over 35 cycles when increasing the electrolyte concentration from 0.2 M to 0.5 M. By measuring the Ca plating-stripping behaviors on various substrates (*i.e.*, glassy carbon, Pt, Cu and Al) and electrolytes (*i.e.*, 0.25 M $Ca[B(hfip)_4]_2$ in THF, DME or diglyme (DGM)),[35] the reversibility of Ca metal was demonstrated to be the best in DGM electrolyte (Fig. 3e), in which the longest lifespan over 300 h was presented (Fig. 3f). These results highlight the importance of solvent selection for stable Ca anodes. The correlations among the ether solvent, anion species and electrochemical behaviours of Ca electrolytes have been thoroughly evaluated by Nathan *et al.*[36] They found that the strong coordination interaction between the ether solvent, such as triglyme, and Ca^{2+} cation does not necessarily enable the reversible calcium deposition. Instead, the strong solvent: Ca^{2+} coordination disabled Ca deposition by destabilizing the coordinating solvent or by frustrating desolvation of the Ca^{2+}. In contrast, in an electrolyte system with weak solvent: Ca^{2+} coordination and well-dissociated anion groups (*i.e.*, $Ca[B(hfip)_4]_2$ in DME), reversible Ca deposition is feasible to occur. This counterintuitive finding provides new insights toward design proper ether electrolytes for Ca metal anodes by tailoring the solvent: anion/cation coordinating behaviours.

The carbonate and ether-based electrolytes mentioned above pose potential challenges of toxicity and flammability. In order to overcome this issue, ionic liquid (IL) electrolyte systems with wide electrochemical stability windows, low vapor pressure, and low flammability as proven in Li and Mg metal batteries,[37–39] have been investigated. As an early attempt, Biria *et al.*[40] dissolved 1 M $Ca(BF_4)_2$ in 1-ethyl-3-methylimidazolium trifluoromethanesulfonate. Although in the CV scans, Ca dissolution and deposition appear at -0.15 and 1.5 V, respectively, Ca||Ca symmetric cells presented high overpotentials near 4 V and low CEs of below 70 %. The poor cyclic performance was ascribed to the SEI layer containing CaF_2, CaS and organic components.[41] Other IL electrolytes containing 1-ethyl-1-

methylpyrrolidinum bis(trifluoromethylsulfonyl) imide ($Pyr_{14}TFSI$) and 1-butylpyrrolidinum bis(trifluoromethylsulfonyl)imide ($Pyr_{H14}TFSI$) were also prepared for Ca metal anodes with large stability windows of about 5.1 V and 3.2 V, respectively.[39] However, since the structural decomposition during co-intercalation of solvated Ca ions, neither of them can be coupled with TiS_2 cathodes with reasonable Ca storage, which limits their application in intercalation CRBs.

In summary, reversible Ca metal anodes have been successfully realized in a series of nonaqueous electrolytes, including $Ca(BF_4)_2$ EC/PC,[26,27] $Ca(BH_4)_2$ THF,[28,29] $Ca[B(hfip)_4]_2$ DME[30,31] and $Ca(BF_4)_2$ ILs.[40] Their performance, in terms of electrolyte component, working electrode, plating/stripping overpotentials, CEs, cycle life and the stability windows, are summarized in Table 1. Although it is not trivial to directly compare the electrode performance under different working conditions, several key implications can be concluded as guidelines to design better electrolytes for Ca metal anodes in the future. (i) So far, Ca anodes exhibit the longest cycle life in $Ca[B(hfip)_4]_2$ DGM electrolyte with a high anodic stability window (up to 5 V), which is very important to high-voltage cathodes.[35] These superior performances appeal $Ca[B(hfip)_4]_2$ electrolytes for viable CRBs. (ii) Precious metal (*i.e.*, Pt and Au) are favorable for Ca plating/stripping. Despite the attractive performance, precious metal electrodes are too expensive to be affordable in practical applications. More studies are required to develop desirable electrolytes for conventional current collectors. (iii) SEI plays a key role in manipulating Ca peeling/plating processes. In new electrolyte systems, the chemical structures of SEI layers have been characterized case by case. However, whether the new SEI components (*i.e.*, CaF_2, CaH_2) are beneficial to Ca deposition is still an open question.[42] (iv) The highest rate capacity reported so far for Ca metal is 8 mA cm^{-2} in Ca||Ca $Ca[B(hfip)_4]_2$ DGM cell with voltage spikes greater than 0.5 V.[35] Although this performance is reasonable for new battery chemistry, it is still far from satisfactory for high-power Ca metal batteries. Overall, future

researches are suggested to design smart electrolytes and favorable interfaces for stable Ca metal anodes.

2.2 Graphite anode

Graphite is one of the most well-known anode materials for commercial LIBs because of the high Li storage capacity, the low intercalation potential and the wide affordability of graphite materials.[43] Graphite has also been considered promising for post-Li ion rechargeable batteries,[44–47] by taking advantage of the knowledge gained from its years of development in commercial LIBs. However, reversible intercalation of Ca^{2+} into graphite is not straightforward. An early study by Emery *et al.*[48] chemically synthesized CaC_6 using highly oriented pyrolytic graphite and molten Li-Ca alloy at 350 ℃. Xu *et al.*[49] also obtained stage-I graphite intercalation compounds (GICs) by mixing graphite powder with Ca in the presence of ethylenediamine at elevated temperatures (25-100 ℃). Nevertheless, none of these studies indicate electrochemical intercalation of Ca^{2+} in graphite at room temperature.

Park *et al.*[50] reported the first reversible (de)intercalation of Ca^{2+} in graphite at room temperature by selecting an appropriate $Ca(BH_4)_2$ dimethylacetamide (DMAc) electrolyte (Fig. 4a). The Ca||graphite cells were galvanostatically discharged/charged at 50 mA g^{-1} between 0.2 and 1.5 V *vs*. Ca^{2+}/Ca. The graphite anode exhibited an initial discharge capacity of 97 mAh g^{-1} and CE of 83.5%, a cyclic capacity of 87 mAh g^{-1} at 100 mA g^{-1} after 50 cycles, and a high rate capacity retention of 75% as the current density increasing from 50 to 2000 mA g^{-1} (Fig. 4b-c). Synchrotron *in-situ* XRD analysis showed that graphite underwent a consecutive staging process during calciation, and the I_c (the lattice distance between two adjacent intercalant layers) values were determined to be 21.2, 17.8 and 14.4 Å for different stages (Fig. 4d). Fourier-transform infrared spectroscopy (FTIR) and ^{13}C nuclear magnetic resonance (NMR) studies confirmed that DMAc solvent molecules were co-intercalated with Ca^{2+} into graphite galleries. The number of DMAc molecule coordinated with one Ca^{2+} was determined to be four by

measuring the weight changes of graphite electrodes at different discharge and charge states. The configuration of the co-intercalated graphite was therefore proposed to be a stage-2 GIC composed of $[Ca\text{-}DMAc_4]^{2+}$ complexes per two graphene sheets (Fig. 4e). Note that the Ca//graphite half-cell presented moderate cyclic stability due to the poor reversibility of Ca metal in DMAc-based electrolyte.

To extend the cycle life of graphite anode, Pyo's group fabricated a coin cell of graphite||$Ca(TFSI)_2$ tetraglyme (TEGDME or G_4) electrolyte||activated carbon.[51] The activated carbon served as the super-capacitive counter electrode to adsorb/desorb $TFSI^-$ during Ca insertion/extraction in graphite, eliminating the complexity and instability of Ca metal anode in $Ca(TFSI)_2$ electrolyte. For long-term cyclic performance, the graphite experienced no noticeable capacity fading after 1000 cycles at 0.5 A g^{-1} and 1 A g^{-1}, respectively. The configuration of the fully intercalated graphite was depicted as a stage 3 GIC with a double-stacked Ca-G_4 complex parallelly inserted per three graphene layers. To estimate the performance of graphite in full Ca-ion batteries, a graphite|| $Ca(TFSI)_2$ G_4 electrolyte|| perylene-3,4,9,10-tetracarbonxylic dianhydride cell was further constructed, which delivered a capacity retention of 80 mAh g^{-1} (based on the cathode mass) for 100 cycles.

Although significant progress has been made in the research of graphite anodes, there are still some fundamental issues remaining. First, the correlation between the feasibility of Ca intercalation and the electrolyte components is elusive. Park *et al*[50] prepared a series of electrolytes for graphite anodes with $Ca(BH_4)_2$, $Ca(BF_4)_2$, $Ca(PF_6)_2$ salts and AN, DGM, THF, EC/PC and DMAc solvents. Interestingly, Ca intercalation only happens in $Ca(BH_4)_2$ DMAc electrolyte. Similarly, in $Ca(TFIS)_2$-based electrolytes,[51] important reaction currents for graphite intercalation were only observed in $Ca(TFIS)_2$ G_4 electrolyte, instead of $Ca(TFIS)_2$ in EC/DMC/EMC, G_1, G_2 and G_3. Both works attributed the electrolyte-dependent Ca intercalation to the strong solvation of Ca^{2+} in specific solvents. However, DFT calculations

revealed stronger solvation energy for Ca-DGM than Ca-DMAc complexes, whereas no Ca intercalation was observed in DGM-based electrolyte. Obviously, understanding of Ca intercalation conditions is still unclear even misleading.[50] Second, the solvated-Ca-ion intercalation induces large volume expansions (*i.e.*, 215% for DMAc-Ca intercalated graphite[50] and 210% for G_4-Ca intercalated graphite[51]). The large volume changes provoke two questions: why does the graphite remain stable during cycles under such large volume variations, and will the large volume variations disintegrate practical batteries? Third, the low Ca ion storage capacity of approximately 80 mAh g^{-1} and the high redox potential of about 0.6 V *vs*. Ca^{2+}/Ca for graphite anode would lead to low energy densities for Ca ion full cells, limiting their practical applications.

2.3 Alloy-type anodes

Alloy anodes have been proven effective in accommodating large amounts of Li^+, Na^+ or K^+ by forming M-alloy (M= metal cations) compounds,[4,52,53] spurring the exploration of Ca-alloy anodes in CRBs. The initial attempt was reported by Lipson *et al.*,[54] who coupled calciated Sn anode and a desodiated manganese hexacyanoferrate cathode into a Ca ion full cell while a low capacity of 40 mAh g^{-1} was presented. Then, in the work to study a Sn||$Ca(PF_6)_2$ EC/PC/DMC/EMC||graphite dual ion battery,[55] Wang *et al.* intensively investigated the phase and stress evolution of a Sn foil anode during calciation/decalciation. The Sn anode was observed to be fully calciated into Ca_7Sn_6 (Fig. 5a) with a high theoretical capacity of 526 mAh g^{-1} and a volume expansion of 136.8%. The crystal structure for Ca_7Sn_6 was depicted as four types of cryptographic structures, in which Ca is surrounded by the six nearest Sn atoms to form a distorted octahedron (Fig. 5b). *In-situ* stress measurements revealed compression stress for Sn foil during the entire calciation/decalciation cycle (Fig. 5c), which is beneficial to prevent the generation and propagation of cracks, thereby ensuring the structural stability of Sn anode. The excellent stability was further evidenced by an elastic-plastic model proposed

by the same group.[56] They argued that the absence of tensile stress at the Sn/$CaSn_x$ interface and the uniform dispersion of compressive stress on Sn foil concertedly enhanced the electrode stability.

Another possible alloy-type anode material is Si. The Si-Ca phase diagram presents a theoretical capacity of 3818 mAh g^{-1} for Ca_2Si. In a DFT study for $CaSi_2$, Ponrouch *et al.*[57] demonstrated that (de-)calciation of $CaSi_2$ is possible at voltages between 1.2 V (formation of metastable de-inserted Si) and 0.57 V (formation of stable fcc-Si) (Fig. 5d). When the fcc-Si was calciated to $CaSi_2$, the average reaction voltage was calculated to be 0.37 V with a volume expansion of 306% and a capacity of 557 mAh g^{-1}. A primary potentiostatic intermittent titration technique (PITT) experiment was conducted at 100 °C for $CaSi_2$ anode, showing a specific capacity of 240 mAh g^{-1} and dealloying/alloying plateaus at 2.75V and 0.88 V *vs.* Ca^{2+}/Ca, respectively (Fig. 5e). After one cycle, unfortunately, the $CaSi_2$ anode failed. No following study was found in the literature for Si anodes, implying the difficulty in pursuing Si anodes for CRBs.

Yao *et al.*[58] designed a four-step screening strategy to filter potential alloy-type anodes for CRBs. In particular, all the binary and ternary Ca intermetallic compounds from Inorganic Crystal Structure Database (ICSD) were identified at the beginning, from which the Ca-metal alloys could be selected. A few metalloids (Si, Sb, Ge), transition metals (Al, Cu, Pb, Bi) and noble metals (Ag, Au, Pt and Pd) were predicted as promising candidates for potential metal-Ca systems by evaluated the reaction voltages, maximum capacities and the energy densities (Fig. 5f-g). These candidates were recommended for further experimental validations.

Compared to the Ca metal and graphite anodes, the alloy-type anodes present limited options (Table 2). Although theoretical studies have forecasted many candidates forming alloy compounds with calcium delivering high capacities and energy densities, few of them have been experimentally validated and typically showing ill-shaped voltage profiles and large

polarizations. For example, the theoretical capacity of $CaSi_2$ is determined to be 557 mAh g^{-1}. Dealloying reactions between Ca and Si have only been claimed at 100 ℃ with a limited capacity of 240 mAh g^{-1},[57] rendering a charge depth of 43 %. Similar low alloying depth was found for a Sn anode, which presents a capacity of 40 mAh g^{-1},[54] referring to 7.5 % of the theoretical capacity of 527 mAh g^{-1}.[55] The incompetence to realize the high theoretical capacities of alloy-type anodes could be attributed to the sluggish kinetics of calciation/decalciation reactions.[59–61] First, the low electronic conductivity of alloy-type anodes, such as Si, would impede rapid charge transfer across the interface. Second, the activation barriers for large Ca^{2+} diffusion in (de)alloyed crystals would be high (*i.e.*, 0.45-2.47 eV for Ca diffusion in Ca_7Sn_6),[58] and therefore lead to slow ion diffusivity in alloy-type anodes. Third, facile Ca^{2+} diffusion would also be retarded by thick SEI layers formed on the surface of alloy-type anodes. The formation of SEI is always associated with low CEs (~80 %)[55] and serious degradation of Ca electrolytes during discharge. It is certain that the ionic diffusivity, alloying depth and volume expansion[62] are critical factors on the path towards design smart alloy-type anodes. Nevertheless, very limited studies have been carried out to elucidate above issues and hence, intensive investigations in these directions are recommended for devising suitable strategies to promote the development of alloy-type anodes in CRBs.

3. Cathode materials

Although anode materials with promising electrochemical performance have been demonstrated, associated with the design of specific non-aqueous electrolytes, CRBs are still far from a commercial reality. This is due to the lack of suitable cathode materials which are expected to deliver high capacities with multivalent redox, high voltages and excellent reversibility in desirable organic electrolytes. In this section, we will provide a rigorous review of the state-of-the-art cathodes in nonaqueous CRBs, including intercalation-type and conversion-type materials.

3.1 Intercalation-type cathodes

Intercalation cathodes refer to materials with an open framework of interconnected sites, wherein the cations can diffuse, and an electronic band structure is able to accept/donor electrons reversibly.[17] Intercalation compounds are the most successful cathode materials for commercial LIBs because of the good cycling stability, fast Li-ion diffusion and the high redox potentials.[63] These compounds are also widely investigated for CRBs. According to the phase-structured materials, the intercalation cathodes can be categorized as layered compounds, transition metal oxides, polyanions, and Prussian blue analogs.

3.1.1 Van der Waals layered compounds

One of the most critical challenges for Ca cathode materials is the slow Ca diffusion kinetics due to the divalent nature and the large size of Ca^{2+}.[17] Van der Waals layered compounds possess two dimensional ionic diffusion channels and weak interlayer forces,[64,65] rendering potentially fast Ca^{2+} diffusion pathways and high structural flexibility.[66,67] Van der Waals layered compounds compromise a large group of materials including layered oxides, sulfides, selenides and MXene, some of them have shown effectiveness in Ca^{2+} storage.

V_2O_5 is a representative layered structure, compromising edge- and corner-sharing VO_5 layers packed through Van der Waals force. Hayashi *et al*[68,69] reported a high Ca storage capacity of ~450 mAh g^{-1} for amorphous V_2O_5 in $Ca(ClO_4)_2$ AN electrolyte. Compared to crystalline V_2O_5, the amorphous phase presented larger capacities and lower overpotentials (Fig. 6a), possibly arising from the isotropic structure of amorphous phase. In addition, DFT calculations presented the thermodynamic stability and Ca migration energy barriers in various V_2O_5 polymorphs.[67,70,71] It showed that the Ca ion diffusion barrier in δ phase (~200 mV) was much lower than in α phase (1700-1900 mV) (Fig. 6c), suggesting δ-CaV_2O_5 is more plausible than α-CaV_2O_5 to reversibly store Ca ion at practical currents. Further DFT studies[72] revealed that the Ca ion diffusion barriers for metastable polymorphs (*i.e.*, 0.56-0.65 eV for δ′-V_2O_5,

0.59-0.68 eV for γ′-V_2O_5 and 0.37-0.55 eV for ρ′-V_2O_5) are substantially lower than those for thermodynamically stable α-V_2O_5 (1.76-1.86 eV), implying possibly high-power capability for metastable V_2O_5 cathodes. It was also found that PC solvent-treated V_2O_5 exhibited a specific capacity of 260 mAh g^{-1}, whereas the dried V_2O_5 cathodes presented a negligible capacity of 20 mAh g^{-1} (Fig. 6b).[73] The difference was attributed to the shielded electrostatic interactions between the Ca^{2+} intercalant and the PC-embed V_2O_5. The similar phenomenon was observed in water-mediated organic electrolyte for V_2O_5 cathodes, where water molecules were inserted to enlarge the interlayer space for V_2O_5.[74,75] Note that this strategy is not desirable in practical CRBs because of the water reduction at high voltages.

Tojo *et al.*[76] evaluated the Ca intercalation performance in orthorhombic MoO_3 (α-MoO_3), another typical Van der Waals layered material composed of octahedral MoO_6 sheets (Fig. 6d). In a $Ca(TFSI)_2$ AN electrolyte, the MoO_3 delivered discharge and charge capacities of 186 and 116 mAh g^{-1}, respectively, rendering a large irreversible capacity of 70 mAh g^{-1}. The irreversible capacity was attributed to the decomposition of electrolyte at the 1st cycle. A minor interlayer expansion from 13.85 to 14.07 Å for MoO_3 after full calciation was detected by *ex-situ* XRD,[77] which is responsible for excellent electrochemical performance. Further, a molybdenum bronze ($Ca_xMoO_3{\cdot}(H_2O)_{0.41}$) was prepared as a stable cathode material with high capacities of 90.7 mAh g^{-1} and 85.3 mAh g^{-1} at the 1st and 50th cycles at 276 mA g^{-1} (Fig. 6e).[78] Unlike the pristine α-MoO_3, molybdenum bronze possesses crystal water between layers (Fig. 6f), which shield the electrostatic force between Ca^{2+} and the host structure, thereby promoting the Ca^{2+} diffusion in $Ca_xMoO_3{\cdot}(H_2O)_{0.41}$.

TiS_2 composed of two hexagonal close-packed sulfide layers has also been investigated as Ca cathodes.[79] The electrochemical intercalation of Ca^{2+} and Mg^{2+} in TiS_2 was compared in carbonated-based electrolytes at 100 °C.[80] Galvanostatic experiments in Ca battery exhibited highly rate-dependent capacities of 520 mAh g^{-1} at C/100 and 210 mAh g^{-1} at C/50, respectively

(Fig. 6g), reflecting the sluggish diffusion of Ca^{2+} in TiS_2. DFT calculations proposed two plausible diffusion pathways for Ca^{2+} in TiS_2 from octahedral to octahedral sites, involving intermediate occupation of the 2*d* tetrahedral site. The energy barrier determined to be 0.75 eV (Fig. 6h) is lower than that the ~1.14 eV for Mg^{2+}, consistent with the negligible Mg storage capacity in TiS_2 under the same conditions. Two new phases for calciated TiS_2 were observed during Ca^{2+} insertion,[81] which were donated as phase 1 and phase 3 with expanded *c* parameters of 27.7 Å and 36.9 Å (comparing to the 5.7 Å for pristine TiS_2), respectively. The huge lattice expansion was attributed to solvated-Ca-ion co-intercalation reaction, similar to the graphite anodes in Section 2.2. Nevertheless, TiS_2 cathodes presented short cycle life, limiting its feasibility as Ca cathodes.

In brief, Van der Waals layered compounds with large interlayer space and weak interlayer forces have been demonstrated practical in accommodating large amounts of Ca^{2+} as potential cathodes. However, the cycle life and reversible capacities are far from satisfactory (Table 3). Several suggestions are provided to improve the performance of this type of Ca cathodes: (i) to utilize co-intercalation reaction to partially shield the strong coulombic interactions between Ca^{2+} and the intercalation hosts, (ii) to fabricate nanostructure cathodes with shortened ion diffusion length and enlarged electrode/electrolyte contact area, and (iii) to expand the lattice parameters with inactive molecules to promote Ca^{2+} migration.

3.1.2 Calcium transition metal oxide compounds

Above we discussed the “traditional” oxides and sulfides with 2D diffusion pathways as Ca hosts. In this part, we will further discuss calcium transition metal oxide compounds (Ca_xMO_2) with different structures as the initial Ca reservoir in CRBs, similar to commercial LIB cathodes (*i.e.*, $LiCoO_2$ and $LiMnO_2$).[82]

Calcium cobaltites (Ca_xCoO_2) ($0.26 \leq x \leq 0.50$) (Fig. 7a) consisting of $[CoO_2]_n$ sheets of edge-sharing octahedral with Ca ions between trigonal prismatic layers represent a class of

cathode materials, which have been successfully synthesized by low temperature ion-exchange of layered Na_xCoO_2.[83] The $Ca_{0.5}CoO_2$ cathode was paired with V_2O_5 anode into a Ca ion full cell in 1 M $Ca(ClO_4)_2$ AN electrolyte.[84] The layered structure was able to deliver reversibly capacities up to 100 mAh g^{-1} under different experimental conditions (*i.e.*, current densities of 30-100 µA and voltage range of 2.3 to -1.2 V). Park *et al.*[85] investigated the thermodynamic stability, theoretical energy capacity, voltage behavior and Ca diffusion barrier of a series of calcium cobaltites, including layered-$CaCo_2O_4$, one dimensional (1D)-$Ca_3Co_2O_6$, brownmillerite-$Ca_2Co_2O_5$ and incommensurate-$[Ca_2CoO_3][CoO_2]_{1.62}$, by DFT simulation and experimental measurements. They found that among the four representative calcium cobaltite structures, layered $CaCo_2O_4$ is the most appealing one with the lowest Ca migration barrier of 0.75 eV, the highest theoretical capacity of 242 mAh g^{-1} (Fig. 7a). The theoretical operation voltage of $CaCo_2O_4$ was calculated to be 3.26 V, lower than the 3.32V for $Ca_3Co_2O_6$ and 3.81 V for $[Ca_2CoO_3][CoO_2]_{1.62}$, which is likely due to the different electronic environment for Co. They further synthesized the $CaCo_2O_4$, $Ca_3Co_2O_6$, and $[Ca_2CoO_3][CoO_2]_{1.62}$ electrodes and tested in $Ca(TFSI)_2$ EC/PC electrolyte but only 2% of the theoretical capacities presented for each cathode without any reversibility. Another phase, perovskite $CaCoO_3$, has also been investigated by DFT, but the Ca migration barrier was calculated to be over 2 eV,[24] preventing any possible Ca extraction.

$CaMn_2O_4$ is another candidate to host Ca^{2+} as the transition metal oxide cathode. Liu *et al.*[23] simulated that the Ca^{2+} mobility barrier (~200-500 meV) in spinel $CaMn_2O_4$ (Fig. 7b) is comparable to that for Li^+ (~400-600 meV) and much lower than that for Mg^{2+} (~600-800 meV) and Zn^{2+} (~850-1000 meV). It implies a high-power capability for spinel $Ca_xMn_2O_4$ in CRBs. In addition, the operation and voltage volumetric capacity for spinel $CaMn_2O_4$ cathode was predicted to be 3.1 V and ~1000 Ah L^{-1}, respectively, whereas a large volume change of over 25% for the spinel phase during Ca insertion/extraction can be produced. Overall, the DFT

calculations judged the virtual spinel $Ca_xMn_2O_4$ a promising cathode material. Unfortunately, Dompablo *et al.*[17] argued that the preference of Ca^{2+} for larger sites makes it thermodynamically impossible to obtain spinel $CaMn_2O_4$ in experimental reality. For $CaMn_2O_4$, marokite phase with Ca in 8-fold coordination sites was regarded as a thermodynamically stable polymorph,[86] presenting a small volume variation of 6% in DFT study.[86] However, the Ca diffusion barrier was calculated to be 1 eV, making it extremely challenging to extract Ca^{2+} under real experimental conditions.

$CaMO_3$ perovskites (M = Mo, Cr, Mn, Fe, Co and Ni) as a structural family of oxides, built up from corner-sharing MO_6 octahedral with cations in the 8-fold coordination sites, have also been explored as potential cathodes by DFT calculations (Fig. 7c).[24] For most perovskite $CaMO_3$ (M= Cr, Mn, Fe, Co and Ni), serious crystal changes with volume expansions above 20 % were predicted during Ca extraction. Only the $CaMoO_3$ was identified structurally possible with a limited volume change of 10% during Ca extraction.[87] Unfortunately, the perovskite $CaMoO_3$ exhibited a high Ca migration barrier of ~2 eV, indicating negligible electrochemical activity in real batteries.

It is evident that the electrochemical inactivity for many transition calcium metal oxides is associated with the high Ca migration energy barriers. The Ca diffusion energies are determined by the diffusion channels in crystal topology as well as the coulombic interactions between Ca^{2+} and the metal cations in the intercalation host. Typically, introduction of negative oxygen and/or Ca vacancies in parent host is likely to reshape the local topology and hence improve the Ca diffusivity. DFT studies of the Ca mobility in oxygen-vacant $Ca_2Fe_2O_5$ and $Ca_2Mn_2O_5$ and Ca-vacant $CaMn_4O_8$, however, showed that the Ca mobility was equally hampered as their parent oxides.[88] Tailoring the oxidation state of transition metal, topologic types based on different transition metal polyhedra or polyhedra arrangements, are accessible to virtual calcium metal oxides cathodes. However, it is not trivial to pinpoint structures

satisfying the topological criteria with reasonable Ca mobilities (≤ 0.525 eV for microparticles and ≤ 0.625 eV for nanoparticles).[89]

Overall, the calcium transition metal oxide compounds are potentially to deliver high voltages and high capacities for Ca cathodes. However, the extremely high Ca diffusion energy barriers and large volume changes are two predominant challenges. In order to evaluate the feasibility of the materials recommended by theoretical studies, experimental studies on the possibility of material preparation, electrolyte compatibility, and the testing protocols are also required.

3.1.3 Polyanion compounds

Polyanion compounds are a big family of materials with a general formula of $AMM'(X_mO_{3m+1})_n$ (A = cation, M,M' =transition metal, X = P, S, Mo or W, $(X_mO_{3m+1})^-$ = tetrahedral polyanion structures).[90] The MO_x polyhedral and X_mO_{3m+1} tetrahedral form a framework with large cation diffusion channels and high thermal stability. In addition, the operation voltage can be tailored by adjusting the local environments of polyanions, endowing them as stable, high voltage and high-power cathode materials in LIB and Na-ion batteries (*i.e.*, $LiFePO_4$ and $Na_3V(PO_4)_3$) and further promising candidates to CRB technology.

$LiFePO_4$ is the most common polyanion cathode in commercial LIBs. $FePO_4$ olivine host has been prepared for Ca^{2+} intercalation by electrochemical removal of Li^+ from $LiFePO_4$ (Fig. 8a).[91] In a $FePO_4$//$Ca(BF_4)_2$ AN//activated carbon cell, the olivine structure presented a Ca storage capacity of 72 mAh g^{-1}, corresponding to ~0.2 mol of Ca^{2+} per $FePO_4$ unit (or approximate 40.5% of the theoretical value) (Fig. 8b). However, the cyclic capacity rapidly degraded to ~28 mAh g^{-1} after 25 cycles at 7.5 mA g^{-1} (Fig. 8c). The poor cyclic performance for $FePO_4$ was also observed in a $FePO_4$//$Ca[B(hfip)_4]_2$ DGM//Ca metal full cell, which only survived 10 cycles at 10 mA g^{-1}.[35]

Na_2FePO_4F is a representative polyanion cathode in Na-ion batteries with plausible Na^+ mobility in the two-dimensional cation diffusion channels and relatively high voltage due to the strong inductive effect of oxygen/fluorine anions.[92] Considering the similar size of Na^+ and Ca^{2+}, Lipson *et al.*[93] intercalated Ca^{2+} into desodiated Na_2FePO_4F ($[]_{1.0}NaFePO_4F$). The average Ca intercalation voltage was 2.6 V *vs.* Ca^{2+}/Ca and the capacity remained approximately 80 mAh g^{-1} (corresponding to $Ca_{0.25}NaFePO_4F$) after 50 cycles at 10 mA g^{-1} in $Ca(PF_6)_2$ EC/PC electrolyte. Recently, Kim *et al.*[91] and Jeon *et al.*[94] independently illustrated the NASICON (natrium super ionic conductor)-structured $NaV_2(PO_4)_3$ prepared by electrochemical removal of Na^+ from $Na_3V_2(PO_4)_3$ as Ca cathodes in nonaqueous electrolytes. The $NaV_2(PO_4)_3$ has an open three-dimensional framework composed of PO_4 tetrahedra and VO_6 octahedra (Fig. 8d), providing enough space for Ca^{2+} migration and accommodation. At a low current density of 3.5 mA g^{-1}, the $NaV_2(PO_4)_3$ cathode delivered an average working plateau voltage of 3.2 V *vs.* Ca^{2+}/Ca and cyclic capacities of about 83 mAh g^{-1} after 40 cycles (Fig. 8e-f),[91] rendering a high energy density of 256 Wh kg^{-1}. Moreover, the Ca storage performance in $NaV_2(PO_4)_3$ was found temperature-dependent.[94] Reversible capacities of 60 and 90 mAh g^{-1} were exhibited for the same cathode cycled at 25 and 75 °C, respectively, which should be attributed to the large energy barrier for Ca diffusion in the structure.

In brief, the above high-voltage and reversible cathode materials suggest that the electrochemical cation exchange method can be used for designing high performance cathodes from existing polyanion compounds for CRBs. Further studies are required to improve the cyclic capacities and pair the stable cathodes with Ca metal for actual high-voltage CRBs.

3.1.4 Prussian blue compounds

Prussian blue (PB) analogs are representative examples of metal organic framework structures and possess the general formula of $A_xM_{Ay}[M_B(CN)_6]_z \cdot nH_2O$, where M_A and M_B are usually Mn, Fe, Co, Ni, Cu or Zn and A is usually Li, Na or K.[95] The large interstitial sites render the PB

analogs capable to store almost all alkali metal ions, thereby they have been intensively investigated in monovalent rechargeable battery cathodes with significant capacities and long cycle life.[96–98] In addition, PB analogs can be synthesized at room temperature in large-scale manners by co-precipitation reactions, making PB compounds cheap and affordable to wide applications.

Lipson *et al.*[54] were the first to use a PB material, manganese hexacyanoferrate ($Na_xMnFe(CN)_6$, designated as MFCN), as the cathode to insert Ca ions in $Ca(PF_6)_2$ EC/PC electrolyte (Fig. 9a). The MFCN was desodiated to create Na vacancies prior to Ca intercalation. The much lower Ca storage capacity of about 75 mAh g^{-1} at 10 mA g^{-1} (Fig. 9b) compared with the discharge capacity in Na-ion cells, suggests the Na vacancies were partially occupied by Ca ions. In Na-ion batteries, both $Mn^{2+/3+}$ and $Fe^{2+/3+}$ participated in redox reactions, while only the $Mn^{2+/3+}$ redox couple was active during cycling in Ca ion batteries leading to the lower electrochemical capacities. A prototype MPCN//calciated Sn full cell was further prepared, which displayed an initial capacity of 80 mAh g^{-1} and a capacity retention of approximately 50% after 35 cycles (Fig. 9c). Possible reasons have been proposed to the short cycling life, such as the delamination of Sn anode from large volume changes, the lack of stable SEI, and the increasing interfacial resistances. Following this study, Lipson *et al.*[99] explored another PB cathode, $NiFe(CN)_6$, which presented a reversible capacity of 60 mAh g^{-1} but degraded rapidly during cycling.

To increase the Ca ion diffusion kinetics in PB analogs, three strategies have been proposed, namely, (i) to enlarge the lattice space, (ii) to reduce the coulombic interaction between Ca^{2+} and the host, and (iii) to increase the operating temperature. An indication to strategies (i) and (ii) is given by Padigi *et al.*,[100] who prepared potassium barium hexacyanoferrate ($K_2BaFe(CN)_6$), in which Ba^{2+} was incorporated to expand the *d*-spacing (Fig. 9d). Galvanic charge-discharge cycling of $K_2BaFe(CN)_6$ presented a negligible capacity of 7.6

mAh g^{-1} in an anhydrous $Ca(ClO_4)_2$ AN electrolyte. In contrast, the reversible capacity was 62 mAh g^{-1} with a high CE of 93.8% after 30 cycles in wet electrolyte by adding 17 % DI water (Fig. 9e). It was explained that the presence of water in the electrolyte enabled hydration and shielding of Ca^{2+}, which facilitated the Ca^{2+} diffusion in $K_2BaFe(CN)_6$ with enlarged *d*-space. Further increasing the water content in electrolyte, the cyclic response was significantly deteriorated, possibly due to the dissolution of active materials in excess amounts of water. For strategy (iii), Shiga *et al.*[101] promoted the electrochemical insertion of Ca^{2+} into $K_{0.1}MnFe(CN)_6$ at 60 ℃. By increasing the working temperature, the desolvation energy of the surrounding ionic solvent may decrease, thus stronger current peaks referring to Ca^{2+} insertion/extraction were observed at 60 ℃ compared to that at 25 ℃.

Although PB analogs have been demonstrated capable in Ca^{2+} storage in non-aqueous electrolytes, their inferior electrochemical performance (*e.g.*, 50 mAh g^{-1} after 30 cycles for $Ca_xMnFe(CN)_6$,[54] 40 mAh g^{-1} after 12 cycles for $K_xNiFe(CN)_6$,[102,103]) make them unacceptable at current stage for practical CRBs. Still, the advantages of low-cost, simple synthesis and wide variety make them promising in stationary storage applications after significant investigations.

3.2 Conversion-type cathodes

Other than intercalation-type cathodes, materials undergoing conversion reaction have also been investigated due to their potentially high theoretical capacities and energy densities from multielectron transfer per redox center. Unlike intercalation cathodes which serve as hosts to accommodate Ca^{2+} without breaking the parent crystallographic or bond structures, the conversion reaction involves the breaking of chemical bonds and formation of new phases. This type of material includes sulfur (S), oxygen (O_2) and organic compounds.

3.2.1 Sulfur

Sulfur has long been considered as a promising cathode material for Li-S batteries,[5,104–107] due to the high theoretical capacity (1675 mAh g^{-1}), high energy density (2600 Wh kg^{-1}), and high

abundance of the raw material. Inspired by the discernible progress in Li-S system, Ca has also been considered appealing to couple with sulfur by delivering two-electron conversion reaction Ca+ S ↔ CaS with a theoretical volumetric capacity of 3202 Wh L^{-1}, which is even higher than the 2800 Wh L^{-1} for a Li-S battery.

In 2013, a primary sulfur/carbon-calcium cell was fabricated with a sulfur-infiltrated mesoporous carbon cathode, a Ca metal anode and a 0.5 M $Ca(ClO_4)_2$ AN electrolyte.[108] The low sulfur utilization and irreversibility of the Ca-S cell with an initial discharge capacity of 600 mAh g^{-1} and a voltage plateau at ~ 0.75 V vs. Ca^{2+}/Ca might be attributed to the incompatibility between Ca metal anode and the $Ca(ClO_4)_2$ AN electrolyte (Fig. 10a). The first reversible Ca-S cell was reported in 2019 by using a $Ca(CF_3SO_3)_2$-$LiCF_3SO_3$ G_4 electrolyte with Ca foil anode, glass-fiber separator, and sulfur/carbon nanofiber cathode.[109]. The Li salt in the Ca electrolyte facilitated the Ca/Li ion diffusion kinetics in electrolyte as well as reactivate the redox products in the Ca-S system. In comparison to the irreversible performance in $Ca(CF_3SO_3)_2$ G_4 electrolyte, these in $Ca(CF_3SO_3)_2$-$LiCF_3SO_3$ G_4 electrolyte presented a remarkable capacity above 1200 mAh g^{-1} and a discharge plateau at 1.2 V for the 1st cycle (Fig. 10b). Cyclic test presented capacities of 800 mAh g^{-1} and 300 mAh g^{-1} at the 1st and 20th cycles with CEs of 95-98% in the bi-salt electrolyte. Soluble polysulfide intermediates (*i.e.*, S_6^{2-} and S_4^{-2}) during calciation were detected, which recalls the shuttling effect of lithium polysulfides in Li-S batteries resulting in fast capacity degradation. Similarly, the calcium polysulfides may also cause the low capacity retention in a Ca-S system.

Promoted by the discovery of reversible Ca plating-stripping in the $Ca[(Bhfip)_4]_2$ DME electrolyte, Zhao-Karger *et al.*[110] fabricated a Ca-S battery with a sulfur/carbon composite cathode, a borate-based electrolyte and a Ca metal anode. CV curves and discharge/charge voltage profiles indicated a typical multistep reaction of Ca-S, that is, sulfur was reduced to high-order Ca polysulfides at 2.2 V and further to solid CaS_2/CaS at 2.08 V and CaS was

oxidized to sulfur at 2.5 V during charging. Although the sulfur cathode delivered a high initial capacity of 760 mAh g^{-1}, the dissolution of polysulfides and the loss of active materials result in a minor capacity of about 120 mAh g^{-1} after 15 cycles (Fig. 10c). The Ca-S reaction behaviors in borate ether electrolyte were further probed by X-ray photoelectron spectroscopy (XPS) and X-ray absorption spectroscopy (XAS) (Fig. 10d).[111] Deconvoluted S 2p, Ca 2p and F 1s XPS spectra of sulfur/carbon cathode and Ca anode at different discharging/charging stages clearly illustrated reversible conversion of sulfur and CaS during calciation and decalciation, accompanied with the generation of CaF_2 and CaS_n byproducts on Ca metal anode. Quantitative analysis of the XPS spectra for cycled Ca anode suggested the formation of mixed calcium boron oxide species at the electrode surface, which might play a critical role in stabilizing the electrolyte/electrode interface and governing the capacity fading during cycles. Operando S K-edge XAS spectra further confirm the reversible conversion among S, CaS_x and CaS (Fig. 10e-f).

Although significant progress has been made for sulfur cathodes in CRBs, it must be noted that the capacity fading is still profound, and the electrochemical activity observed at high sulfur content is negligible. These challenges are probably related to both the fundamental issues for sulfur cathodes such as the stability of sulfur cathode, polysulfide shuttling effect, and the compatibility of electrolyte/electrode and the specific issues of Ca-S systems, including the reversibility of sulfur species to coordinate Ca^{2+} and the difficulty in activation of sulfur and calcium sulfides during cycling. Insightful understandings and smart cathode structures are both of importance to promote the Ca-S system closer to practical use.

3.2.2 Other conversion cathodes

Ca-O_2 battery offers theoretical energy densities of over 1000 Wh L^{-1} by two-electron transfer per O_2/O^{2-} redox. However, few attentions have been paid to Ca-O_2 systems due to two barriers: (i) the discharge product, calcium oxides, was difficult to be decomposed at ambient

temperature, and (ii) few organic electrolytes can simultaneously meet the requirements of a suitable working window and reversible dissolution/deposition of Ca metal. Reinsberg *et al.*[112] investigated the oxygen reduction in Ca^{2+} dimethyl sulfoxide electrolyte on Au, glassy carbon, Pt and Ru electrodes by using differential electrochemical mass spectroscopy to observe the formation and oxidization of superoxide while this work did not realize the recycling of a Ca-O_2 cell. By using 2,2,6,6-tetramethylpiperidine 1-oxyl (TEMPO) catalyst for the cathode, Ca metal anode and an ionic liquid electrolyte, Shiga *et al.*[113] reported the first rechargeable Ca-O_2 battery with the 1st discharge/charge capacities of 1802 mAh g^{-1} and 1409 mAh g^{-1}, respectively, at a discharge voltage of 1.8 V (Fig. 11a-b). Although the Ca-O_2 battery decayed rapidly after several cycles due to the severe passivation of Ca metal in ionic liquid electrolytes, it claimed the feasibility of developing reversible Ca-O_2 chemistry, especially by combining the most recent advances in Ca metal anodes in Section 2.1 and the strategies established for O_2 cathodes in Li-O_2 batteries.

Organic electrode materials offer possibly high electrochemical capacities with a multitude of cations through conversion and absorption reactions owning multielectron redox capability. Organic electrodes can be divided into three classes based on reaction mechanisms: N-type through reduction and storage of cations, P-type via oxidation and storage of anions, and these using both mechanisms.[114] N-type cathodes are the most practical counterpart for metal anodes, allowing operation in lean electrolyte for practically high energy densities. Despite several organic materials have been reported to store Ca^{2+} in aqueous electrolytes,[13,115] very few investigations appear for organic cathodes in nonaqueous CRBs. Bitenc *et al.*[116] tested a poly(anthraquinoyl sulphide) (PAQS) against a Ca metal anode using $Ca[B(hfip)_4]_2$ DME electrolyte in two- or three-electrode cells. The PAQS/CNT composite cathode delivered a high capacity of 169.3 mAh g^{-1} at 0.2 C, which is 75 % of the theoretical value (225 mAh g^{-1}), confirming a significant utilization degree of active materials (Fig. 11c). However, the capacity

decreased rapidly to 112.3 mAh g^{-1} after 6 cycles and then failed. Both the capacity fade at the cathode and the increase of overpotentials at the Ca anode were responsible for the fast capacity decay (Fig. 11d), and the latter contributed more as evidenced by the three-electrode cell tests. By reviewing the current situation of organic compounds as conversion cathodes in CRBs, it is clear that high capacity cathodes are achievable while there is plenty of room to optimize both the electrode structures with appropriate electrolytes.

4. Performance assessment and mechanism analysis

4.1 Performance assessment

Tables 1-3 summarize the electrode materials and their electrochemical performance discussed above, from which one can clearly observe the discernible progress in CRBs research, associated with improvements in both anode and cathode materials. The achievements and existing challenges for performance are discussed as follows.

For anode materials, new electrolytes have been formulated for reversible Ca metal. Among the exiting carbonate-, ether-, IL- and gel-based electrolytes, the borate $Ca[B(hfip)_4]_2$ DME seems the most promising with a high anodic stability (up to 5 V) and hundreds of Ca plating-stripping cycles at low overpotentials (<0.5 V) (Table 1)[31,32,35]. Ca//S[111] and Ca//PAQS[116] full cells have been realized in $Ca[B(hfip)_4]$ DME electrolyte with high reversible capacities. However, Ca metal anodes in the borate electrolyte are still struggling with the formation and growth of passivation films, leading to unsatisfactory cycle life for full cells (*e.g.*, 15 cycles for Ca//S battery[111] and 6 cycles for Ca//PAQS battery[116]). Non-Ca metal anodes, such as graphite and Sn (Table 2), provide promising alternatives to flee the complex obstacles from Ca metal. Graphite is capable of delivering surprisingly long cycle life (2000 cycles in $Ca(TFSI)_2$ G_4 electrolyte)[51] and high power capability (75% capacity retention from 50 to 2000 mA g^{-1})[50], both of which are favorable to high power and long life CRBs, along with the benefit of low-cost for graphite materials. Nevertheless, more efforts are required to

improve the Ca intercalation capacity, decrease the redox potential, and alleviate the large volume expansion of graphite during Ca co-intercalation reactions. In brief, high capacity and long-life Ca metal and graphite anodes in CRBs are dawning.

Different from the gratifying progress in anode materials, most of the reported cathodes present short cycle life (<100 cycles), low capacities (<100 mAh g^{-1}) and poor rate capabilities (Table 3). The inferior cathode performance can be attributed to the fundamental challenges (*i.e.*, large and divalent Ca^{2+}, depressed cation diffusion kinetics, and large volume change of hosts), the irreversibility of counter electrodes (*i.e.*, Sn[99] and Ca[111]) and the poor electrolyte compatibility.[85] Despite the frustrating performance at current stage, the stimulus can still be identified from the knowledge gained. First, high-voltage cathodes can be expected from the polyanion and transition metal oxide compounds (*i.e.*, $CaMn_2O_4$,[23] $CaCo_2O_4$,[85] and $NaV_2(PO_4)_3$[91]). Second, high capacities are achievable for conversion cathode materials undergoing multi-electron redox reactions. The representative example is sulfur, which has delivered one of the highest reversible capacities over 900 mAh g^{-1}.[111] Third, long life cathodes have been observed for Van der Waals layered compounds (*i.e.*, 500 cycles for $Mg_{0.25}V_2O_5{\bullet}H_2O$[14]), due to their rigid open framework and large cation diffusion channels. Although excellent performance has been achieved separately, how to integrate the properties of high voltage, high capacity and long life into one cathode material is still challenging. In addition, the reliability of experimental setup, the electrolyte/electrode computability and the stability of passivating layers also matter. All the above factors shall be comprehensively examined towards eventual application of CRB with feasible cathodes.

Taken the above achievements and challenges into account, the merits of CRBs can be evaluated in respect of energy density and cost, which are the initial motivations to CRB study. The operation potential *vs.* gravimetric and volumetric energy densities were calculated for some existing or virtual electrodes for CRBs by Palacin *et al.* using the energy-cost model

developed by Berg et al.(Fig. 12)[16,117]. Ca metal batteries with moderate operating voltages (2-3.5V) and capacities (100-300 mAh g^{-1}) from intercalation cathodes would yield higher specific energy densities than the state-of-the-art LIBs and Na-ion batteries (Fig. 12a). The larger density of Ca than that of Li leads to higher volumetric energy density for Ca-S batteries than Li-S technology (Fig. 12b), which enables Ca-S battery to penetrate the application scenarios with limited space, *e.g.*, military niche. For cost comparison, the Ca price (Ca metal costs are foreseen 5-50 \$ kg^{-1})[117] is much lower than that of Li (Li metal of about 100 \$ kg^{-1}).[20] As a result, Ca metal batteries could possess superior cost-effectiveness to the state-of-the-art $LiNi_{0.33}Mn_{0.33}Co_{0.33}O_2$ (NMC)//graphite LIBs (110\$ per KWh with energy densities of 279 Wh kg^{-1} and 711 Wh L^{-1}).[118] For instance, if the high voltage $CaCo_2O_4$ (3.26 V with a theoretical capacity of 241 mAh g^{-1}) is approachable, energy densities of about 390 Wh kg^{-1} and 1350 Wh L^{-1} can be calculated for Ca//$CaCo_2O_4$ full cell (assuming the full cell with 50% excess Ca anode, standard electrode components and similar cost for $CaCo_2O_4$ and NMC),[117] enabling the energy cost close to 60 \$ per kWh, which is near half of the NMC/graphite LIBs. The price merit would be particularly attractive to large-scale energy storage applications.

4.2 Mechanism analysis

Fundamental findings related to cathode materials and electrolytes for CRBs have been recently summarized by Palacin *et al.*[17] and Gallant *et al.*[42]. To avoid duplication, in this work, we will focus on the most recent discoveries in Ca metal anodes and interfaces. It is worth noting that the importance of the compatibility between electrolytes and electrode materials should never been understated. The success of both electrodes is hinged on the electrolyte components, because both the salt and solvent influence the reversibility of Ca metal anodes, and the anions in electrolyte affect the oxidation stability of the electrolyte which in turn limits the choice of high voltage cathodes.

One of the biggest motivations of CRB study is the possibility to use the high volumetric capacity Ca metal as safe anode. Endorsed by the reputation of Mg metal anode, Ca metal plating has long been regarded as non-dendritic[9]. Various morphologies, including dense and thick film,[28] discrete grains[27,29] and aggregates of spherical structures,[30] have been reported for Ca plating. The diverse plating morphologies call for cautions when considering them as anode materials. Thanks to the advanced liquid *in-situ* transmission electron microscopy (TEM) technique, the nucleation and growth of Ca metal in $Ca(BH_4)_2$ THF electrolyte become visible at nanoscale (Fig. 13a).[119] When plating at moderate current densities ranging from 1 to 10 mA cm^{-2}, Ca uniformly deposited on Pt electrode in globular growth, whereas, tree-like Ca dendrites and "dead" Ca generated aggressively at 100 mA cm^{-2} (Fig. 13b). The current density-dependent transition from globular-to-dendrite growth is consistent with the conventional model proposed for Li metal anodes, that the ion diffusion rate is insufficient to compensate the ion deposition rate at high current densities, with the loss of equilibrium and causing dendrite formation.[120] Further *in-situ* TEM observation of Ca plating at 1 mA cm^{-2} then 10 mA cm^{-2} presented an overall globular morphology but Ca dendrite at a closer examination (Fig. 13c). It was interpreted that the presence of irregular SEI layers pre-formed at 1 mA cm^{-2} induced local high-current concentration spots, which assisted the dendrite growth. This work suggests the importance of current densities and SEI on governing Ca-dendrite formation.

Another critical challenge to Ca metal plating is the passivation film formed on Ca metal surface.[18] Characterizations claimed different chemical compositions on Ca metal surface cycled in different electrolytes, such as CaH_2 for $Ca(BH_4)_2$ THF electrolyte[28] and CaF_2 for $Ca[B(hfip)_4]_2$ DME electrolyte.[31] The correlation between the nature of passivation layer and the Ca plating behavior is unknown. Ponrouch *et al.*[121] recently placed an effort to unveil the role of the passivation layer on Ca deposition. By analyzing the SEI components on Ca metal cycled in $Ca(BF_4)_2$ EC/PC and $Ca(TFSI)_2$ EC/PC electrolytes, they found that the former

sample was rich in borates/organic-rich compounds while the latter was carbonate-based compound. DFT calculations showed that many calcium compounds (*i.e.*, CaF_2, CaO, $CaCO_3$, $Ca_2B_2O_5$) presented Ca^{2+} migration barriers exceeding 1000 meV, which is too high to allow practical Ca^{2+} percolation. To ascertain if the organic-rich interfaces generated in $Ca(BF_4)_2$ EC/PC are more appealing to Ca^{2+} diffusion, stainless steel electrodes were pre-covered with a borate containing layer. The pre-treated electrode presented important Ca plating current when cycling in the $Ca(TFSI)_2$ EC/PC electrolyte (Fig. 13d). Note that direct cycling of Ca in $Ca(TFSI)_2$ EC/PC is irreversible. This work inspires to design Ca-ion conducting artificial interfaces to facilitate Ca plating.[122,123] As a proof-of-concept, Song *et al.*[124] demonstrated an ultralong-life Ca metal anode by engineering a Na/Ca hybrid SEI (Fig. 13e). The hybrid SEI containing Na_2O and CaF_2 was formed by cycling Ca//Ca symmetric cells in $NaPF_6$ EC/DMC/EMC electrolyte. The Na_2O nanocrystals surrounded by amorphous phases were accounted for the protective effect of SEI in alleviating the anion oxidation of Ca deposit as well as promoting the Ca^{2+} penetration. Indeed, the artificial engineering strategy has been developed in Li metal and Mg metal anodes to prevent electrolyte decomposition and ensure rapid diffusion of cations. Lessons learned from previous successes are recommended to promote the development of Ca metal anodes via customizing interfacial components.

5. Conclusions and perspectives

The studies reviewed and summarized in this work provide an overall picture of the state of the art of various aspects of CRBs. For anodes, a variety of new electrolytes have been validated for reversible Ca stripping and plating at room temperature. The electrolyte-Ca metal interfaces as well as the electrochemical stability of electrolytes have been investigated, which are important prerequisites for Ca-metal batteries. Non-Ca metal anodes, like graphite and Sn, have shown to deliver high power capability (*i.e.*, the co-intercalation graphite anode) and high capacities (*i.e.*, the alloying Sn anode). For cathodes, both intercalation and conversion cathode

materials are known to deliver an encouraging performance with high voltage, high capacity, and long life. Based on the progress and challenges summarized in this work, we propose the following perspectives for the future development of CRBs (Fig. 14):

(1) It is essential to design appropriate testing protocols and cell configurations with rigorous electrochemical characterizations methods. For a new battery system, the electrolyte decomposition and current collector corrosion can contribute to the current flow and should be taken into account. On the other hand, some cathodes may present a complete absence of or poor electrochemical activity. The electrochemical inactivity can be attributed to the electrode materials, the passivation of the Ca metal reference/counter electrode interface, the incompatibility of the electrode with the electrolyte, and the unsuitability of cell configurations. Obtaining precise characterization insights for unambiguous results for new battery systems is challenging because of a lack of standardization. To prevent misinterpretation of electrochemical results of Ca-based batteries, we provide the following suggestions: (i) three-electrode setups should be more widely exploited to obtain accurate information; (ii) electrochemical characterization should always be accompanied by the structural characterization of the cycled electrode materials to obtain as much information as possible for deducing the underlying mechanisms, and (iii) *operando* characterizations, such as *in-situ* TEM and *in-situ* XRD, should be further developed to examine the detailed structural evolution in the electrodes during operation. Thus, reliable cell configurations and rigorous characterizations constitute the foundation for studying new electrode materials in CRBs.

(2) The hunt for new and advanced electrode materials would benefit tremendously through a combination of computational and experimental investigations. Theoretical simulations can be used to examine the electrode materials in terms of the Ca^{2+} diffusion energy barriers, reaction potentials, thermodynamic stability, and electronic structures of intermediates. Furthermore, with the emerging artificial intelligence (AI) technology, virtual materials with ideal

electrochemical properties to satisfy specific requirements can be generated. Constructing high-throughput computational databases coupled with AI can significantly simplify interpreting experimental results. More advanced characterization techniques, including *in-situ*/*ex-situ* synchrotron X-ray diffraction, neutron diffraction, nuclear magnetic resonance spectroscopy, secondary ion mass spectroscopy, and electron microscopy, can be employed to obtain integrated, three-dimensional images of structural evolution of cathodes in CRBs. In-depth experimental studies can verify some theoretical hypothesis from computational studies. The combination of elaborate computational tools and powerful experimental studies can accelerate the development of CRBs.

(3) Advanced electrode structures can be obtained by structural engineering methods such as nanotechnology, which can provide a large accessible surface area for short ion diffusion length, high charge transfer rate, and high tolerance towards volume variations (*i.e.*, alloying-type anodes and conversion cathodes for CRBs). Given the high charge density and sluggish Ca^{2+} diffusion in intercalation cathodes, chemical structural design, including cationic disordering, partial cation reduction, and manipulation of intrinsic defects are also powerful strategies to improve electrochemical performance. Another approach is surface modification, like carbon coating, which can improve the electrical conductivity, limit the volume change, maintain structural integrity, and provide stable interfaces. Moreover, excellent reversibility of both electrodes in an electrolyte solution involves developing optimized interfacial layers and CEs of electrode materials, especially for the Ca metal anode. More studies should be devoted to exploring suitable electrolytes with a large electrochemical stability window, moderate ion dissociation energy, and appropriate physical properties. Furthermore, the compatibility of the electrodes and the electrolytes at different working conditions, such as extreme temperatures, are also important.

(4) To achieve commercial CRB technology, various engineering aspects need to be considered, which include, but are not limited to, the cell/battery configuration design, the anode-cathode mass/capacity balance, the optimization of the electrolyte content, the mass loading, and the proportion of inactive components. Additionally, upscaling of material fabrication and battery manufacturing, from laboratory to commercial scale, poses significant challenges. The environmental friendliness of the devices should also be seriously considered before promoting any practical application. CRBs offer the potential for energy storage for large-scale stationary and propulsion applications. However, the development of the CRB technology is still in its infancy, even when compared to other multivalent battery chemistries like the Mg ion battery. Nevertheless, the increasing research interest and the encouraging progress offer a promising path to success.

Conflicts of interest

There are no conflicts to declare.

Acknowledgements

The work described in this paper was supported by a grant from the Research Committee of The Hong Kong Polytechnic University under project code 1-BE3M, 1-W179 and 1-BBXK. Z.L.X thanks the invaluable suggestions from Prof. Y Yao at Huston University in USA during the manuscript preparation.

Note and Reference

1 M. Armand and J.-M. Tarascon, *Nature*, 2008, **451**, 652–657.

2 D. Larcher and J.-M. Tarascon, *Nat. Chem.*, 2015, **7**, 19–29.

3 S. W. Kim, D. H. Seo, X. Ma, G. Ceder and K. Kang, *Adv. Energy Mater.*, 2012, **2**, 710–721.

4 Z. L. Xu, X. Liu, Y. Luo, L. Zhou and J. K. Kim, *Prog. Mater. Sci.*, 2017, **90**, 1–44.

5 Z. L. Xu, J. K. Kim and K. Kang, *Nano Today*, 2018, **19**, 84–107.

6 Z. L. Xu, J. Park, G. Yoon, H. Kim and K. Kang, *Small Methods*, 2018, **8**, 1800227.

7 J. W. Choi and D. Aurbach, *Nat. Rev. Mater.*, 2016, **1**, 1–16.

8 A. Ponrouch, J. Bitenc, R. Dominko, N. Lindahl, P. Johansson and M. R. Palacin, *Energy Storage Mater.*, 2019, **20**, 253–262.

9 Y. Liang, H. Dong, D. Aurbach and Y. Yao, *Nat. Energy*, 2020, **5**, 646–656.

10 D. Aurbach, Z. Lu, A. Schechter, Y. Gofer, H. Gizbar, R. Turgeman, Y. Cohen, M. Moshkovich and E. Levi, *Nature*, 2000, **407**, 724–727.

11 M. C. Lin, M. Gong, B. Lu, Y. Wu, D. Y. Wang, M. Guan, M. Angell, C. Chen, J. Yang, B. J. Hwang and H. Dai, *Nature*, 2015, **520**, 325–328.

12 L. E. Blanc, D. Kundu and L. F. Nazar, *Joule*, 2020, **4**, 771–799.

13 S. Gheytani, Y. Liang, F. Wu, Y. Jing, H. Dong, K. K. Rao, X. Chi, F. Fang and Y. Yao, *Adv. Sci.*, 2017, **4**, 1–7.

14 X. Xu, M. Duan, Y. Yue, Q. Li, X. Zhang, L. Wu, P. Wu, B. Song and L. Mai, *ACS Energy Lett.*, 2019, **4**, 1328–1335.

15 R. J. Gummow, G. Vamvounis, M. B. Kannan and Y. He, *Adv. Mater.*, 2018, **30**, 1801702.

16 A. Ponrouch and M. R. Palacin, *Curr. Opin. Electrochem.*, 2018, **9**, 1–7.

17 M. E. Arroyo-de Dompablo, A. Ponrouch, P. Johansson and M. R. Palacín, *Chem. Rev.*, 2020, **120**, 6331–6357.

18 D. Aurbach, R. Skaletsky and Y. Gofer, *J. Electrochem. Soc.*, 1991, **138**, 3536–3545.

19 P. Canepa, G. Sai Gautam, D. C. Hannah, R. Malik, M. Liu, K. G. Gallagher, K. A. Persson and G. Ceder, *Chem. Rev.*, 2017, **117**, 4287–4341.

20 L. Stievano, I. de Meatza, J. Bitenc, C. Cavallo, S. Brutti and M. A. Navarra, *J. Power Sources*, 2021, **482**, 228875.

21 T. R. Juran and M. Smeu, *J. Power Sources*, 2019, **436**, 2–7.

22 T. R. Juran, J. Young and M. Smeu, *J. Phys. Chem. C*, 2018, **122**, 8788–8795.

23 M. Liu, Z. Rong, R. Malik, P. Canepa, A. Jain, G. Ceder and K. A. Persson, *Energy Environ. Sci.*, 2015, **8**, 964–974.

24 M. E. Arroyo-De Dompablo, C. Krich, J. Nava-Avendaño, M. R. Palacín and F. Bardé, *Phys. Chem. Chem. Phys.*, 2016, **18**, 19966–19972.

25 R. J. Staniewicz, *J. Electrochem. Soc.*, 1980, **127**, 782.

26 A. Ponrouch, C. Frontera, F. Bardé and M. R. Palacín, *Nat. Mater.*, 2016, **15**, 169–172.

27 S. Biria, S. Pathreeker, H. Li and I. D. Hosein, *ACS Appl. Energy Mater.*, 2019, **2**, 7738–7743.

28 D. Wang, X. Gao, Y. Chen, L. Jin, C. Kuss and P. G. Bruce, *Nat. Mater.*, 2018, **17**, 16–20.

29 K. Ta, R. Zhang, M. Shin, R. T. Rooney, E. K. Neumann and A. A. Gewirth, *ACS Appl. Mater. Interfaces*, 2019, **11**, 21536–21542.

30 Y. Jie, Y. Tan, L. Li, Y. Han, S. Xu, Z. Zhao, R. Cao, X. Ren, F. Huang, Z. Lei, G. Tao, G. Zhang and S. Jiao, *Angew. Chemie*, 2020, **132**, 12789–12793.

31 Z. Li, O. Fuhr, M. Fichtner and Z. Zhao-Karger, *Energy Environ. Sci.*, 2019, **12**, 3496–3501.

32 A. Shyamsunder, L. E. Blanc, A. Assoud and L. F. Nazar, *ACS Energy Lett.*, 2019, **4**, 2271–2276.

33 Z. Zhao-Karger, M. E. Gil Bardaji, O. Fuhr and M. Fichtner, *J. Mater. Chem. A*, 2017, **5**, 10815–10820.

34 N. T. Hahn, J. Self, T. J. Seguin, D. M. Driscoll, M. A. Rodriguez, M. Balasubramanian, K. A. Persson and K. R. Zavadil, *J. Mater. Chem. A*, 2020, **8**, 7235–7244.

35 K. V. Nielson, J. Luo and T. L. Liu, *Batter. Supercaps*, 2020, **3**, 766–772.

36 N. T. Hahn, D. M. Driscoll, Z. Yu, G. E. Sterbinsky, L. Cheng, M. Balasubramanian and K. R. Zavadil, *ACS Appl. Energy Mater.*, 2020, **3**, 8437–8447.

37 G. A. Giffin, *J. Mater. Chem. A*, 2016, **4**, 13378–13389.

38 I. Osada, H. De Vries, B. Scrosati and S. Passerini, *Angew. Chemie - Int. Ed.*, 2016, **55**, 500–513.

39 T. Stettner, R. Dugas, A. Ponrouch and A. Balducci, *J. Electrochem. Soc.*, 2020, **167**, 100544.

40 S. Biria, S. Pathreeker, F. S. Genier, H. Li and I. D. Hosein, *ACS Appl. Energy Mater.*, 2020, **3**, 2310–2314.

41 S. Biria, S. Pathreeker, F. S. Genier and I. D. Hosein, *ACS Appl. Polym. Mater.*, 2020, **2**, 2111–2118.

42 A. M. Melemed, A. Khurram and B. M. Gallant, *Batter. Supercaps*, 2020, **3**, 570–580.

43 R. Yazami, K. Zaghib and M. Deschamps, *J. Power Sources*, 1994, **52**, 55–59.

44 M. Moshkovich, Y. Gofer and D. Aurbach, *J. Electrochem. Soc.*, 2001, **148**, E155.

45 Z.-L. Xu, G. Yoon, K.-Y. Park, H. Park, O. Tamwattana, S. J. Kim, W. M. Seong and K. Kang, *Nat. Commun.*, 2019, **10**, 2598.

46 J. Park, Z.-L. Xu and K. Kang, *Front. Chem.*, 2020, **8**, 1–14.

47 I. Muhammad, U. Younis, W. Wu, H. Xie, A. Khaliq and Q. Sun, *J. Power Sources*, 2020, **480**, 228876.

48 N. Emery, C. Hérold and P. Lagrange, *J. Solid State Chem.*, 2005, **178**, 2947–2952.

49 W. Xu and M. M. Lerner, *Chem. Mater.*, 2018, **30**, 6930–6935.

50 J. Park, Z.-L. Xu, G. Yoon, S. K. Park, J. Wang, H. Hyun, H. Park, J. Lim, Y.-J. Ko, Y. S. Yun and K. Kang, *Adv. Mater.*, 2020, **32**, 1904411.

51 S. J. Richard Prabakar, A. B. Ikhe, W. B. Park, K. Chung, H. Park, K. Kim, D. Ahn, J. S. Kwak, K.-S. Sohn and M. Pyo, *Adv. Sci.*, 2019, **6**, 1902129.

52 H. Kim, H. Kim, Z. Ding, M. H. Lee, K. Lim, G. Yoon and K. Kang, *Adv. Energy Mater.*, 2016, **6**, 1600943.

53 T. Ramireddy, R. Kali, M. K. Jangid, V. Srihari, H. K. Poswal and A. Mukhopadhyay, *J. Electrochem. Soc.*, 2017, **164**, A2360–A2367.

54 A. L. Lipson, B. Pan, S. H. Lapidus, C. Liao, J. T. Vaughey and B. J. Ingram, *Chem. Mater.*, 2015, **27**, 8442–8447.

55 M. Wang, C. Jiang, S. Zhang, X. Song, Y. Tang and H. M. Cheng, *Nat. Chem.*, 2018, **10**, 667–672.

56 N. Wu, W. Yao, X. Song, G. Zhang, B. Chen, J. Yang and Y. Tang, *Adv. Energy Mater.*, 2019, **9**, 1803865.

57 A. Ponrouch, D. Tchitchekova, C. Frontera, F. Bardé, M. E. A. De Dompablo and M. R. Palacín, *Electrochem. commun.*, 2016, **66**, 75–78.

58 Z. Yao, V. I. Hegde, A. Aspuru-Guzik and C. Wolverton, *Adv. Energy Mater.*, 2019, **9**, 1802994.

59 H. Tan, D. Chen, X. Rui and Y. Yu, *Adv. Funct. Mater.*, 2019, **29**, 1808745.

60 M. Li, J. Lu, X. Ji, Y. Li, Y. Shao, Z. Chen, C. Zhong and K. Amine, *Nat. Rev. Mater.*, 2020, **5**, 276–294.

61 J. Niu, Z. Zhang and D. Aurbach, *Adv. Energy Mater.*, 2020, **10**, 2000697.

62 T. T. Tran and M. N. Obrovac, *J. Electrochem. Soc.*, 2011, **158**, A1411.

63 M. Mao, T. Gao, S. Hou and C. Wang, *Chem. Soc. Rev.*, 2018, **47**, 8804–8841.

64 G. G. Amatucci, F. Badway, A. Singhal, B. Beaudoin, G. Skandan, T. Bowmer, I. Plitz, N. Pereira, T. Chapman and R. Jaworski, *J. Electrochem. Soc.*, 2001, **148**, A940.

65 J. Carrasco, *J. Phys. Chem. C*, 2014, **118**, 19599–19607.

66 T. N. Vo, H. Kim, J. Hur, W. Choi and I. T. Kim, *J. Mater. Chem. A*, 2018, **6**, 22645–22654.

67 M. S. Chae, J. W. Heo, J. Hyoung and S. T. Hong, *ChemNanoMat*, 2020, **6**, 1049–1053.

68 M. Hayashi, H. Arai, H. Ohtsuka and Y. Sakurai, *J. Power Sources*, 2003, **119**–**121**, 617–620.

69 M. Hayashi, H. Arai, H. Ohtsuka and Y. Sakurai, *Electrochem. Solid-State Lett.*, 2004, **7**, 119–121.

70 G. S. Gautam, P. Canepa, R. Malik, M. Liu, K. Persson and G. Ceder, *Chem. Commun.*, 2015, **51**, 13619–13622.

71 R. Verrelli, A. P. Black, C. Pattanathummasid, D. S. Tchitchekova, A. Ponrouch, J. Oró-Solé, C. Frontera, F. Bardé, P. Rozier and M. R. Palacín, *J. Power Sources*, 2018, **407**, 162–172.

72 A. Parija, D. Prendergast and S. Banerjee, *ACS Appl. Mater. Interfaces*, 2017, **9**, 23756–23765.

73 M. Bervas, L. C. Klein and G. G. Amatucci, *Solid State Ionics*, 2005, **176**, 2735–2747.

74 Y. Murata, S. Takada, T. Obata, T. Tojo, R. Inada and Y. Sakurai, *Electrochim. Acta*, 2019, **294**, 210–216.

75 L. Liu, Y.C. Wu, P. Rozier, P.-L. Taberna and P. Simon, *Research*, 2019, **2019**, 1–11.

76 T. Tojo, H. Tawa, N. Oshida, R. Inada and Y. Sakurai, *J. Electroanal. Chem.*, 2018, **825**, 51–56.

77 M. Cabello, F. Nacimiento, R. Alcántara, P. Lavela, C. Pérez Vicente and J. L. Tirado, *Chem. Mater.*, 2018, **30**, 5853–5861.

78 M. S. Chae, H. H. Kwak and S. T. Hong, *ACS Appl. Energy Mater.*, 2020, **3**, 5107–5112.

79 C. Lee, Y. T. Jeong, P. M. Nogales, H. Y. Song, Y. S. Kim, R. Z. Yin and S. K. Jeong, *Electrochem. commun.*, 2019, **98**, 115–118.

80 D. S. Tchitchekova, A. Ponrouch, R. Verrelli, T. Broux, C. Frontera, A. Sorrentino, F. Bardé, N. Biskup, M. E. Arroyo-De Dompablo and M. R. Palacín, *Chem. Mater.*, 2018,

30, 847–856.

81 R. Verrelli, A. Black, R. Dugas, D. Tchitchekova, A. Ponrouch and M. R. Palacin, *J. Electrochem. Soc.*, 2020, **167**, 070532.

82 P. He, H. Yu, D. Li and H. Zhou, *J. Mater. Chem.*, 2012, **22**, 3680–3695.

83 B. L. Cushing and J. B. Wiley, *J. Solid State Chem.*, 1998, **141**, 385–391.

84 M. Cabello, F. Nacimiento, J. R. González, G. Ortiz, R. Alcántara, P. Lavela, C. Pérez-vicente and J. L. Tirado, *Electrochem. commun.*, 2016, **67**, 59–64.

85 H. Park, Y. Cui, S. Kim, J. T. Vaughey and P. Zapol, *J. Phys. Chem. C*, 2020, **124**, 5902–5909.

86 M. E. A. De Dompablo, C. Krich, J. Nava-Avendaño, N. Biškup, M. R. Palacín and F. Bardé, *Chem. Mater.*, 2016, **28**, 6886–6893.

87 M. Baldoni, L. Craco, G. Seifert and S. Leoni, *J. Mater. Chem. A*, 2013, **1**, 1778–1784.

88 A. Torres, F. J. Luque, J. Tortajada and M. E. Arroyo-de Dompablo, *Energy Storage Mater.*, 2019, **21**, 354–360.

89 Z. Rong, R. Malik, P. Canepa, G. Sai Gautam, M. Liu, A. Jain, K. Persson and G. Ceder, *Chem. Mater.*, 2015, **27**, 6016–6021.

90 Z. Gong and Y. Yang, *Energy Environ. Sci.*, 2011, **4**, 3223–3242.

91 S. Kim, L. Yin, M. H. Lee, P. Parajuli, L. Blanc, T. T. Fister, H. Park, B. J. Kwon, B. J. Ingram, P. Zapol, R. F. Klie, K. Kang, L. F. Nazar, S. H. Lapidus and J. T. Vaughey, *ACS Energy Lett.*, 2020, **5**, 3203–3211.

92 Y. Kawabe, N. Yabuuchi, M. Kajiyama, N. Fukuhara, T. Inamasu, R. Okuyama, I. Nakai and S. Komaba, *Electrochem. commun.*, 2011, **13**, 1225–1228.

93 A. L. Lipson, S. Kim, B. Pan, C. Liao, T. T. Fister and B. J. Ingram, *J. Power Sources*, 2017, **369**, 133–137.

94 B. Jeon, J. W. Heo, J. Hyoung, H. H. Kwak, D. M. Lee and S.-T. Hong, *Chem. Mater.*,

2020, **32**, 8772–8780.

95 B. Wang, Y. Han, X. Wang, N. Bahlawane, H. Pan, M. Yan and Y. Jiang, *iScience*, 2018, **3**, 110–133.

96 P. Nie, L. Shen, H. Luo, B. Ding, G. Xu, J. Wang and X. Zhang, *J. Mater. Chem. A*, 2014, **2**, 5852–5857.

97 C. Zhang, Y. Xu, M. Zhou, L. Liang, H. Dong, M. Wu, Y. Yang and Y. Lei, *Adv. Funct. Mater.*, 2017, **27**, 1604307.

98 Y. Lu, L. Wang, J. Cheng and J. B. Goodenough, *Chem. Commun.*, 2012, **48**, 6544–6546.

99 A. L. Lipson, S. D. Han, S. Kim, B. Pan, N. Sa, C. Liao, T. T. Fister, A. K. Burrell, J. T. Vaughey and B. J. Ingram, *J. Power Sources*, 2016, **325**, 646–652.

100 P. Padigi, G. Goncher, D. Evans and R. Solanki, *J. Power Sources*, 2015, **273**, 460–464.

101 T. Shiga, H. Kondo, Y. Kato and M. Inoue, *J. Phys. Chem. C*, 2015, **119**, 27946–27953.

102 T. Tojo, Y. Sugiura, R. Inada and Y. Sakurai, *Electrochim. Acta*, 2016, **207**, 22–27.

103 N. Kuperman, P. Padigi, G. Goncher, D. Evans, J. Thiebes and R. Solanki, *J. Power Sources*, 2017, **342**, 414–418.

104 Z.-L. Xu, J.-Q. Huang, W. G. Chong, X. Qin, X. Wang, L. Zhou and J.-K. Kim, *Adv. Energy Mater.*, 2017, **7**, 1602078.

105 Z.-L. Xu, S. Lin, N. Onofrio, L. Zhou, F. Shi, W. Lu, K. Kang, Q. Zhang and S. P. Lau, *Nat. Commun.*, 2018, **9**, 4164.

106 Z.-L. Xu, S. J. Kim, D. Chang, K.-Y. Park, K. S. Dae, K. P. Dao, J. M. Yuk and K. Kang, *Energy Environ. Sci.*, 2019, **12**, 3144–3155.

107 Z.-L. Xu, N. Onofrio and J. Wang, *J. Mater. Chem. A*, 2020, **6**, 15828–15838.

108 K. A. See, J. A. Gerbec, Y. S. Jun, F. Wudl, G. D. Stucky and R. Seshadri, *Adv. Energy Mater.*, 2013, **3**, 1056–1061.

109 X. Yu, M. J. Boyer, G. S. Hwang and A. Manthiram, *Adv. Energy Mater.*, 2019, **9**, 1803794.

110 Z. Li, B. P. Vinayan, T. Diemant, R. J. Behm, M. Fichtner and Z. Zhao-Karger, *Small*, 2020, **16**, 1–6.

111 A. Scafuri, R. Berthelot, K. Pirnat, A. Vizintin, J. Bitenc, G. Aquilanti, D. Foix, R. Dedryvère, I. Arčon, R. Dominko and L. Stievano, *Chem. Mater.*, 2020, **32**, 8266–8275.

112 P. Reinsberg, C. J. Bondue and H. Baltruschat, *J. Phys. Chem. C*, 2016, **120**, 22179–22185.

113 T. Shiga, Y. Kato and Y. Hase, *J. Mater. Chem. A*, 2017, **5**, 13212–13219.

114 J. Xie and Q. Zhang, *Small*, 2019, **15**, 1805061.

115 M. Adil, A. Sarkar, A. Roy, M. R. Panda, A. Nagendra and S. Mitra, *ACS Appl. Mater. Interfaces*, 2020, **12**, 11489–11503.

116 J. Bitenc, A. Scafuri, K. Pirnat, M. Lozinšek, I. Jerman, J. Grdadolnik, B. Fraisse, R. Berthelot, L. Stievano and R. Dominko, *Batter. Supercaps*, 2021, **4**, 214–220.

117 D. Monti, A. Ponrouch, R. B. Araujo, F. Barde, P. Johansson and M. R. Palacín, *Front. Chem.*, 2019, **7**, 1–6.

118 E. J. Berg, C. Villevieille, D. Streich, S. Trabesinger and P. Novák, *J. Electrochem. Soc.*, 2015, **162**, A2468–A2475.

119 S. D. Pu, C. Gong, X. Gao, Z. Ning, S. Yang, J. J. Marie, B. Liu, R. A. House, G. O. Hartley, J. Luo, P. G. Bruce and A. W. Robertson, *ACS Energy Lett.*, 2020, **5**, 2283–2290.

120 A. Hagopian, M.-L. Doublet and J.-S. Filhol, *Energy Environ. Sci.*, 2020, **13**, 5186–5197.

121 J. Forero-Saboya, C. Davoisne, R. Dedryvère, I. Yousef, P. Canepa and A. Ponrouch, *Energy Environ. Sci.*, 2020, **13**, 3423–3431.

122 H. Song, J. Su and C. Wang, *Adv. Energy Mater.*, 2021, **11**, 2003685.

123 A. M. Melemed and B. M. Gallant, *J. Electrochem. Soc.*, 2020, **167**, 140543.

124 H. Song, J. Su and C. Wang, *Adv. Mater.*, 2020, 2006141.

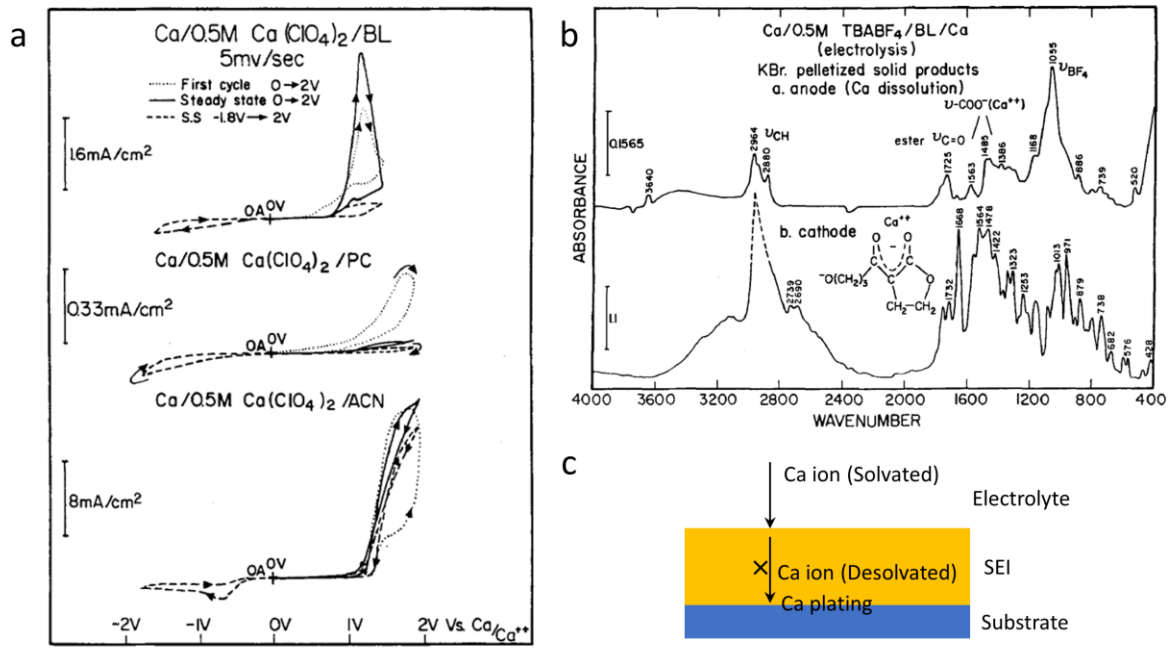

Figure 1 (a) CV curves obtained with Ca electrodes and $Ca(ClO_4)_2$ electrolyte, showing the infeasibility of reversible Ca stripping and plating in a few organic electrolytes, (b) FTIR of surface species formed on Ca plating, showing Ca ion blocking passivation layers[18], (c) schematic illustration of the difficulty in Ca plating process. Reprinted with permission from (a, b)[18], copyright 1991 Electrochemical Society.

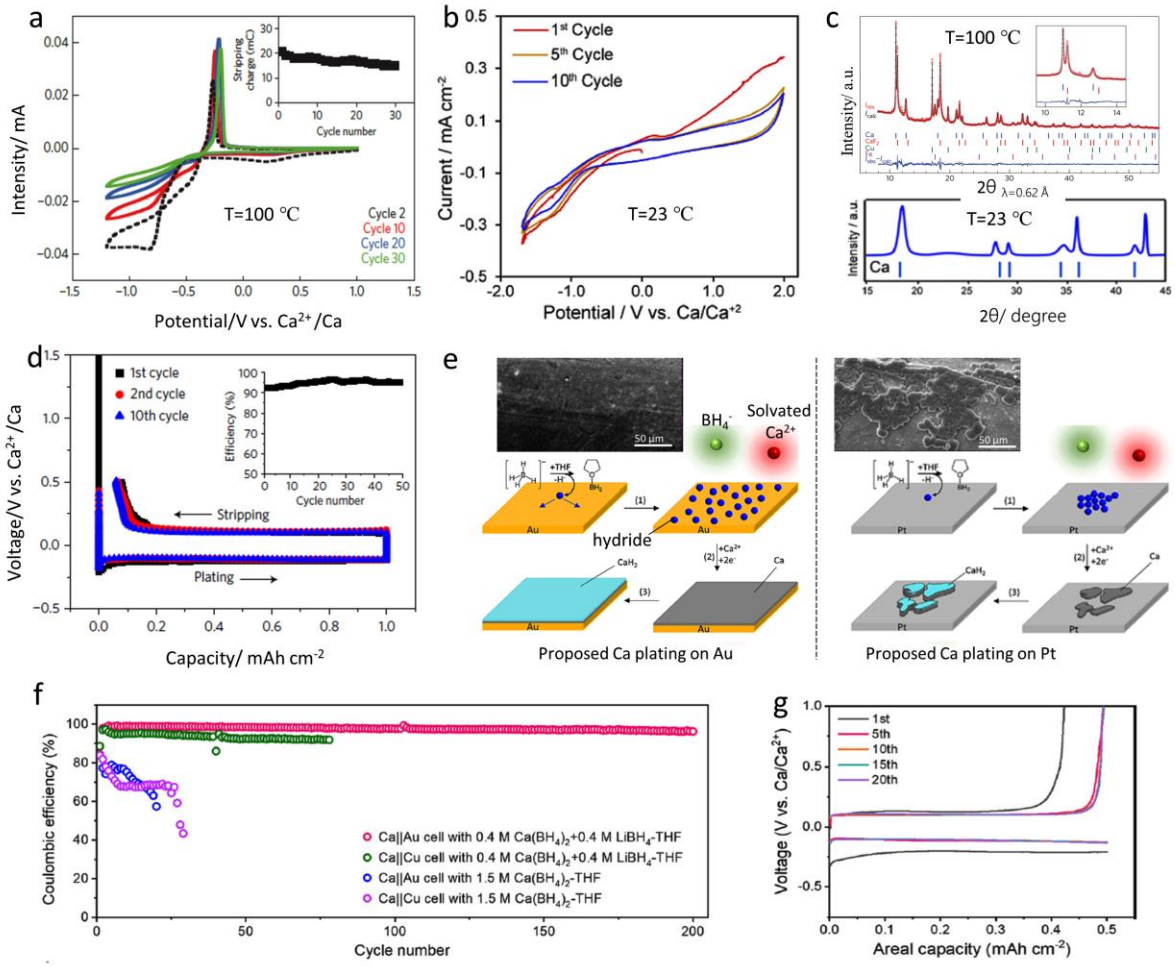

Figure 2 Reversible Stripping/plating of Ca metal in $Ca(BF_4)_2$ EC/PC electrolyte at (a) 100 ℃ for 30 cycles[26] and (b) 23 ℃ for 10 cycles[27], (c) XRD patterns of deposited Ca in (a, b) [26,27]; (d) galvanostatic cycling of Ca metal in 1.5 M $Ca(BH_4)_2$ THF electrolyte at room temperature[28], (e) schemes of proposed Ca deposition on Au and Pt electrodes in $Ca(BH_4)_2$ THF electrolyte[29]; (f) coulombic efficiencies of Ca//Au and Ca//Cu cells in $Ca(BH_4)_2$-$LiBH_4$-THF and $Ca(BH_4)_2$-THF electrolytes and (g) voltage profiles of selected cycles on Au electrode in $Ca(BH_4)_2$-$LiBH_4$-THF electrolyte.[30] Reprinted with permission from (a, c)[26], copyright 2016 Nature publishing group, (b, c)[27] copyright 2019 American Chemical Society, (d)[28] copyright 2018 Nature publishing group, (e)[29] copyright 2019 American Chemical Society, (f, g)[30] copyright 2020 WILEY-VCH GmbH, Weinheim.

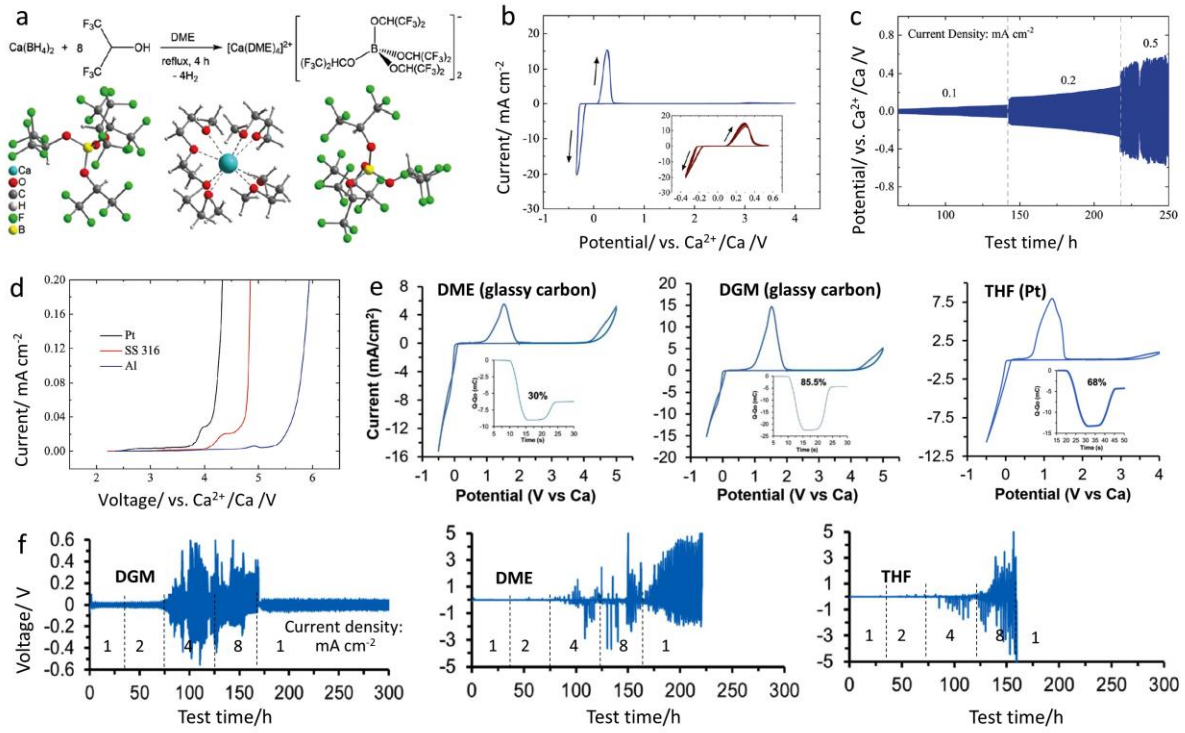

Figure 3 (a) Synthesis of $Ca[B(hfip)_4]_2$ salt, (b) CV curves of Ca plating/stripping in the $Ca[B(hfip)_4]_2$/DME electrolyte at a scan rate of 80 mV s^{-1}, (c) the cycling performance of Ca//Ca cell in $Ca[B(hfip)_4]_2$/DME at different currents, and (d) oxidative stability of $Ca[B(hfip)_4]_2$/DME on stainless steel, Pt and Al;[31] (e) CV curves of Ca stripping and plating on glassy carbon, Pt electrodes with $Ca[B(hfip)_4]_2$ DME, DGM and THF electrolytes, (f) Ca symmetric cells cycling in $Ca[B(hfip)_4]_2$ DGM, DME and THF electrolytes from 1 to 8 mA cm^{-2}.[35] Reprinted with permission from (a-d),[31] copyright 2019 Royal Chemical Society, (e-f)[35] copyright 2020 WILEY-VCH GmbH, Weinheim.

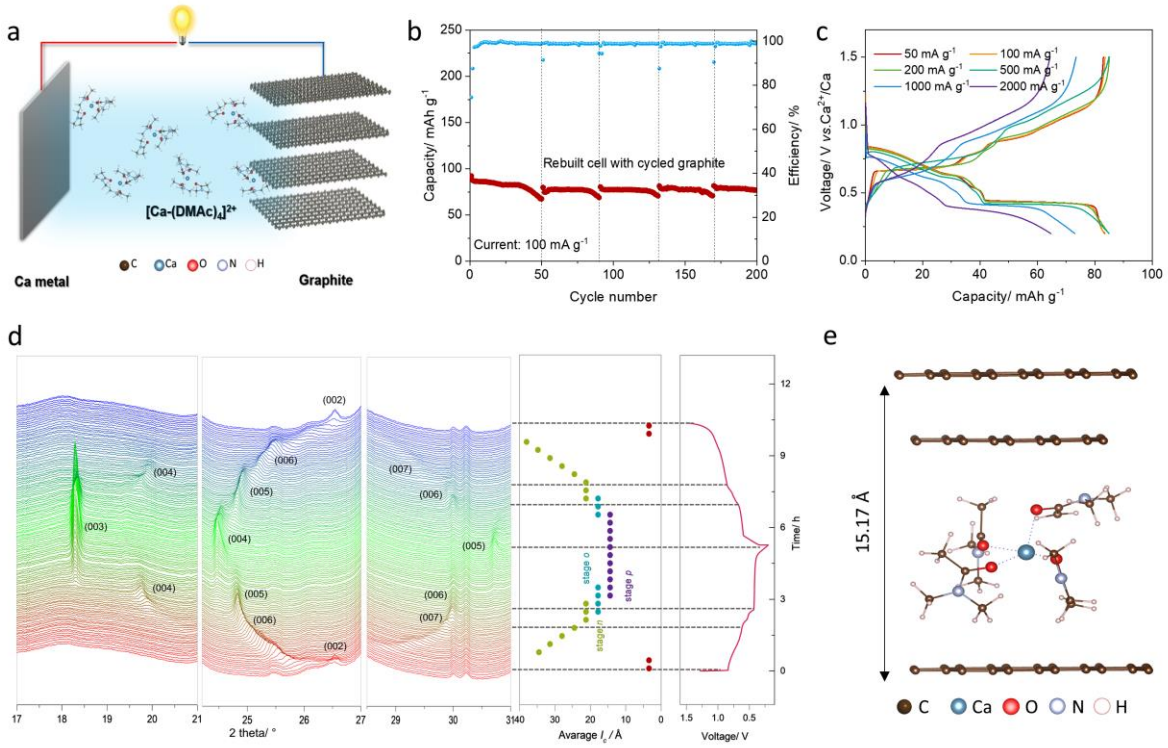

Figure 4 (a) Schematic illustration of Ca ion intercalation in graphite, (b) cyclic capacities at 100 mA g^{-1}, (c) voltage profiles at current densities ranging from 50 to 2000 mA g^{-1}, (d) synchrotron in-situ XRD analysis of the structural evolution of graphite during calciation and decalciation, (e) DFT simulated configuration of $[Ca(DMAc)_4]^{2+}$ intercalated graphite.[50] Reprinted with permission from (a-e),[50] copyright 2020 WILEY-VCH GmbH, Weinheim.

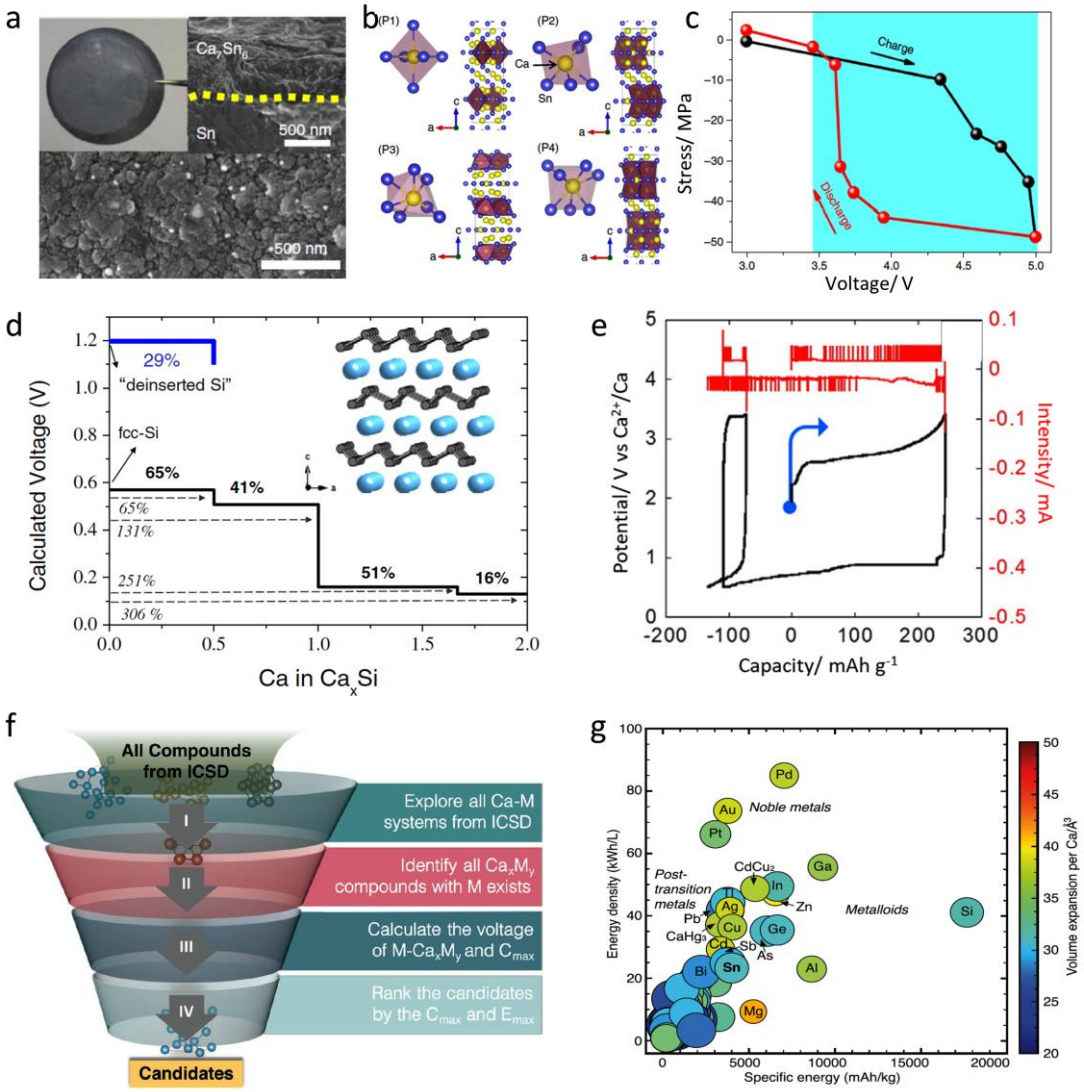

Figure 5 (a) SEM images of cycled Sn foil, (b) schematic of four bonding situations for Ca_7Sn_6, (c) *in-situ* stress measurement of a Sn anode during alloying and dealloying processes;[55] (d) simulated voltage-composition profiles for Si anodes in the Ca-Si alloys, (e) electrochemical performance of $CaSi_2$ anode in PITT test at 100 °C;[57] (f) screening Ca-metal alloy anodes using HT-DFT calculations, (g) HT-DFT screening results for high performance Ca-metal anodes with restrictive voltage constraint, in terms of energy density and volume expansions.[58] Reprinted with permission from (a-c),[55] copyright 2018 Nature publishing group, (d, e),[57] copyright 2016 Elsevier, (f, g)[58] copyright 2019 WILEY-VCH GmbH, Weinheim.

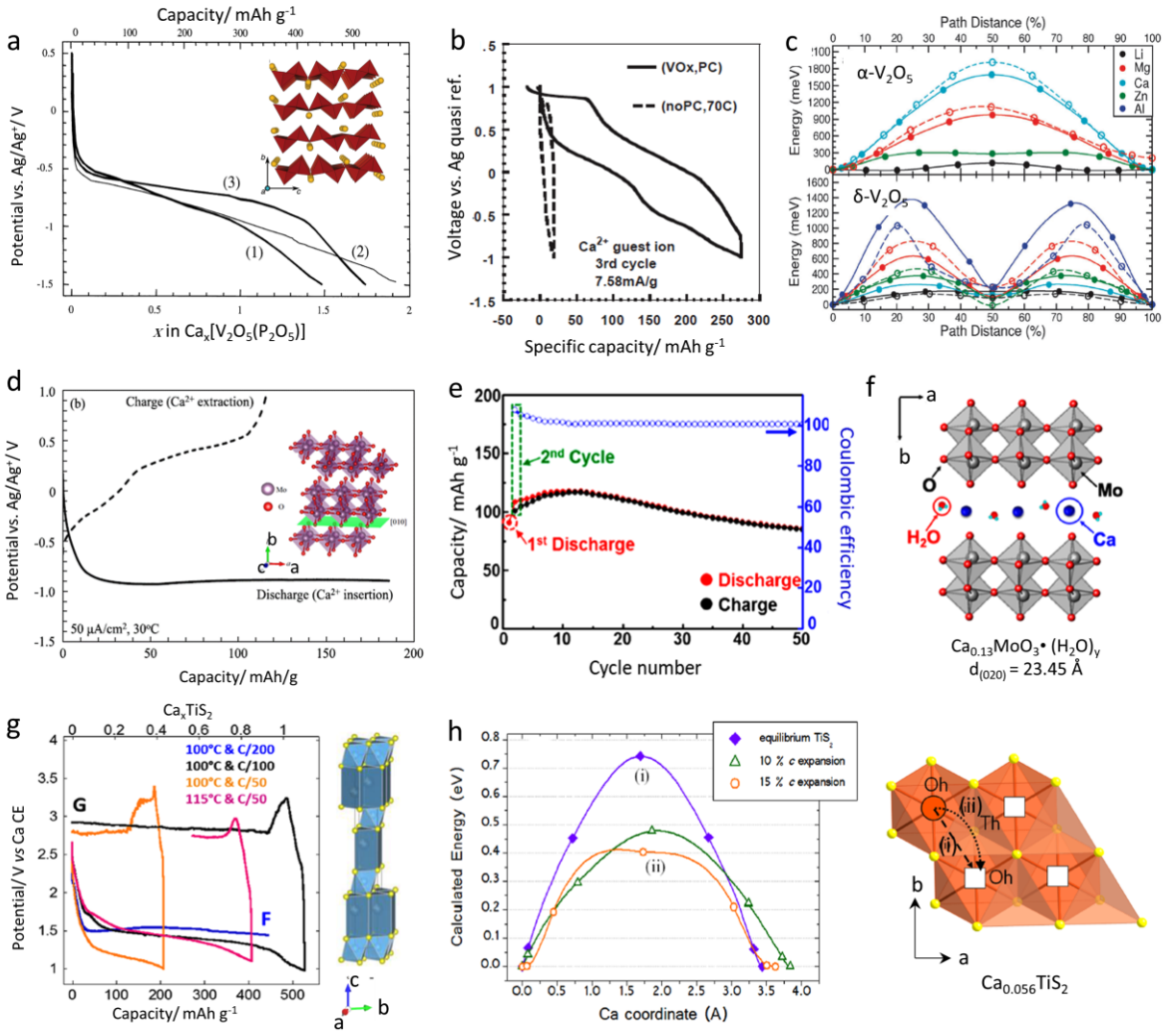

Figure 6 (a) Discharge curves of (1) c-V_2O_5, (2) a-V_2O_5 and (3) a-V_2O_5-P_2O_5 in 1 M $Ca(ClO_4)_2$ AN electrolyte,[68] (b) VO_x and VO_x-PC cycled in $Ca(ClO_4)_2$ PC electrolyte,[73] (c) activation barriers for the cation diffusion (*i.e.*, Ca) in α- and δ-V_2O_5,[70] (d) voltage-capacity profile for α-MoO_3 (inset),[76] (e) cyclic performance and (f) structure for $Ca_xMoO_3 \cdot H_2O$ cathodes;[78] (g) voltage-capacity profiles of TiS_2 at different temperatures and current densities, (h) Ca diffusion energy barriers and routes in TiS_2 (right).[80] Reprinted with permission from (a, b),[68,73] copyright 2003, 2005 Elsevier, (c)[70] copyright 2015 Royal Chemical Society, (d)[76], copyright 2018 Elsevier, (e-h)[78,80] copyright 2018, 2020 American Chemical Society.

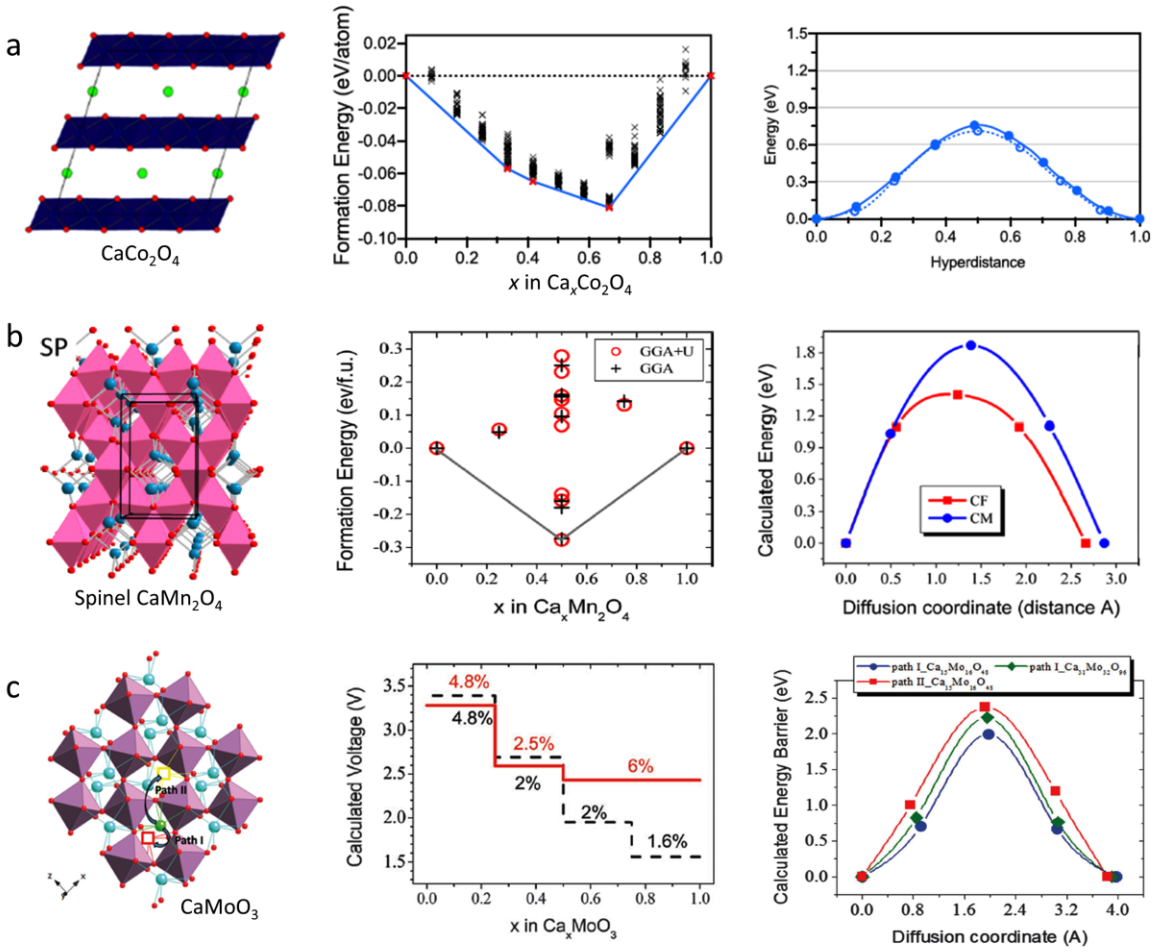

Figure 7 (a) The structure, calculated formation energy convex hull and the Ca diffusion energy barriers for $CaCo_2O_4$,[85] (b) schematic structure, calculated formation energy convex hull and the energy barrier for Ca diffusion for spinel $CaMn_2O_4$,[23] (c) structure, Ca diffusion paths, calculated voltage-composition curve and the energy barrier for Ca diffusion for $CaMoO_3$.[24] Reprinted with permission from (a-c),[23,24,85] copyright 2016, 2020 American Chemical Society.

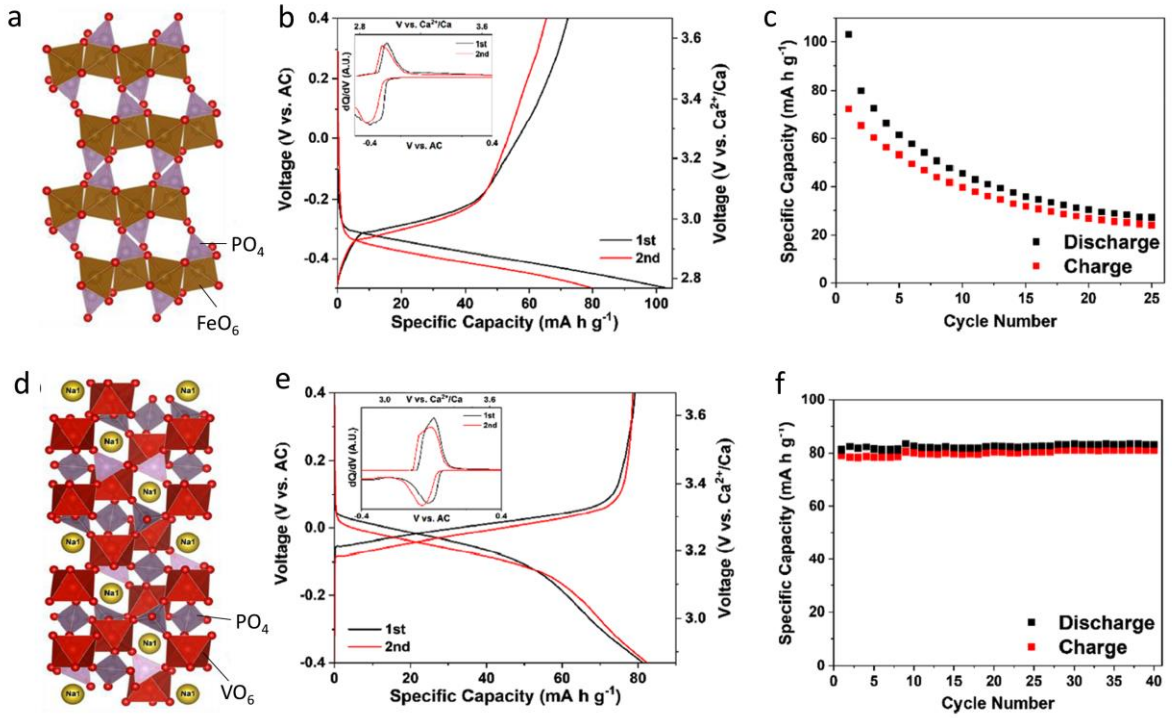

Figure 8 (a) Structure, (b) capacity-voltage and dQ/dV (inset) profiles and (c) cyclic capacities at 7.5 mA g^{-1} for $FePO_4$ cathode; (d) structure, (e) capacity-voltage and dQ/dV (inset) profiles and (c) cyclic capacities at 3.5 mA g^{-1} for $NaV_2(PO_4)_3$ cathode.[91] Reprinted with permission from (a-f),[91] copyright 2020 American Chemical Society.

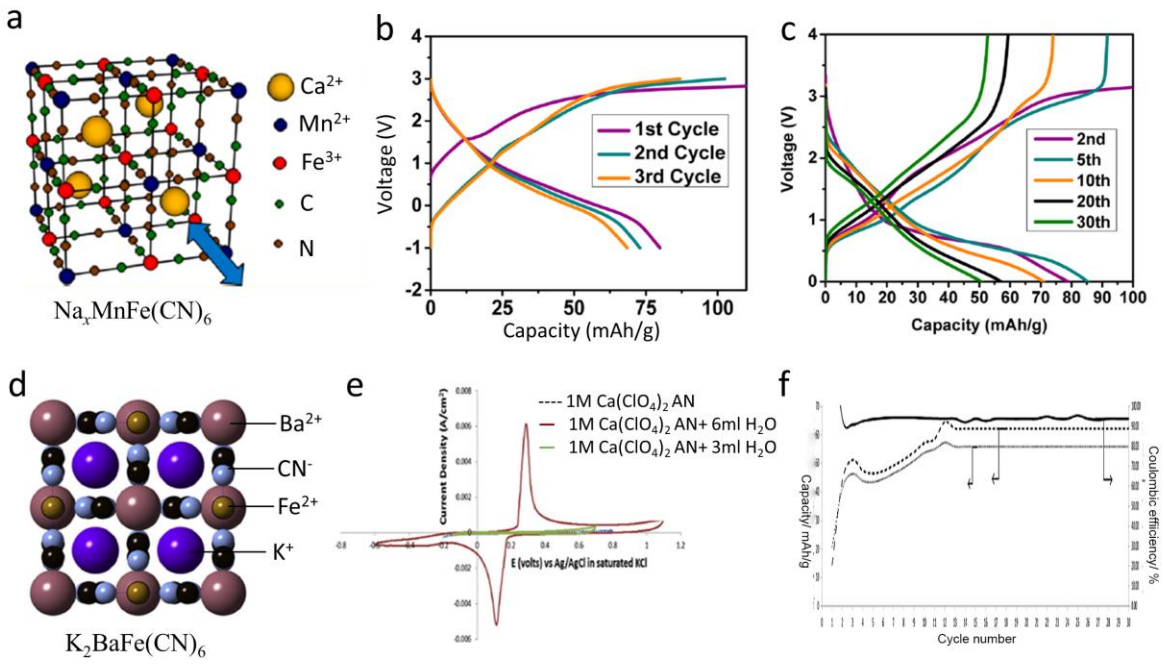

Figure 9 (a) Structure of $Na_xMnFe(CN)_6$ (MFCN) PB cathode, (b) galvanostatic discharge-charge curves for MFCN in 0.2M $Ca(PF_6)_2$ EC/PC electrolyte, (c) voltage profiles of MFCN//Sn full cell for 30 cycles at 10 mA g^{-1},[54] (d) structure of $K_2BaFe(CN)_6$ PB cathode, (e) CV curves in 1 M $Ca(ClO_4)_2$ AN electrolyte with different amount of water, (f) cyclic capacities in 1M $Ca(ClO_4)_2$ AN + 6 ml water electrolyte.[100] Reprinted with permission from (a-c),[54] copyright 2015 American Chemical Society, (d-f)[100] copyright 2015 Elsevier.

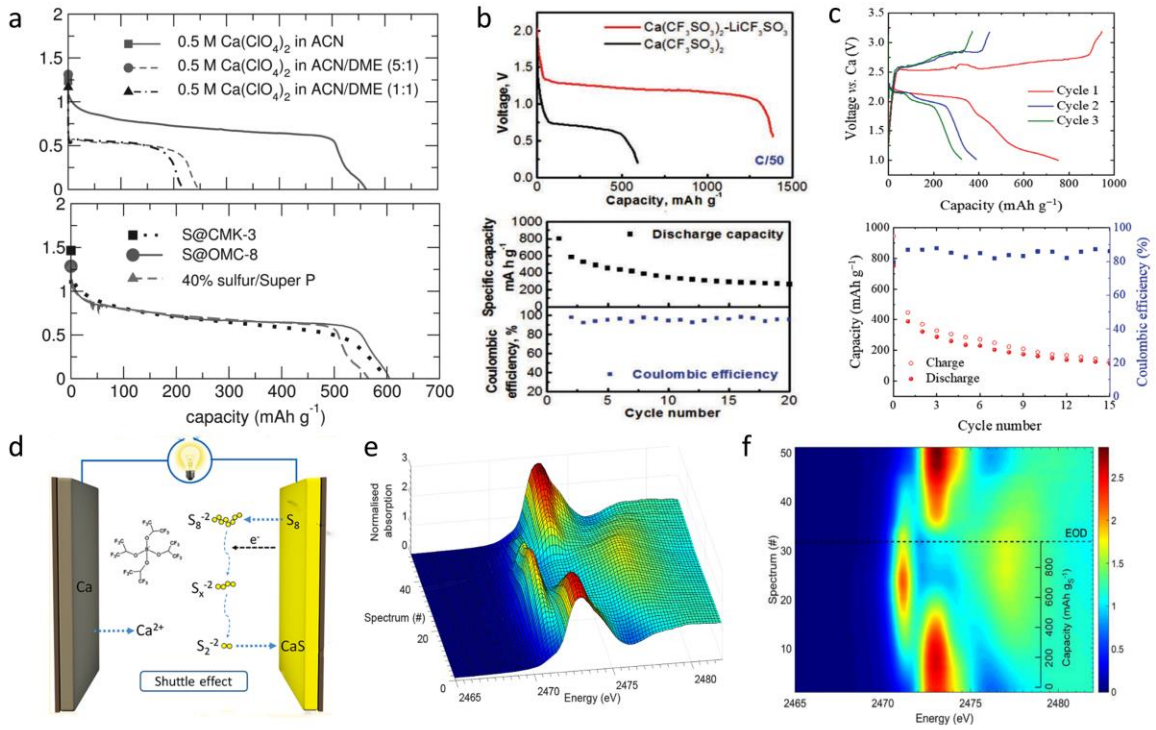

Figure 10 Electrochemical performance and working principle for Ca-S batteries. (a) A primary Ca-S battery with initial discharge profiles using different electrolytes and sulfur/carbon cathodes,[108] (b) a secondary Ca-S battery using bi-salt $Ca(CF_3SO_3)_2$-$LiCF_3SO_3$ G_4 electrolyte (up) with improved cyclic capacities and coulombic efficiencies (down),[109] (c) charge/discharge voltage profiles (up) and cyclic performance (down) of a Ca-S battery with $Ca[B(hfip)_4]_2$/DME electrolyte,[110] (d) schematic illustration of the working mechanism of a Ca-S battery, (e) 3D and (f) topographic view of operando S K-edge XANES spectra during one cycle of a Ca-S battery.[111] Reprinted with permission (a-c),[108–110] copyright 2013, 2019, 2020 WILEY-VCH GmbH, Weinheim, (d-f)[111], copyright 2020 American Chemical Society.

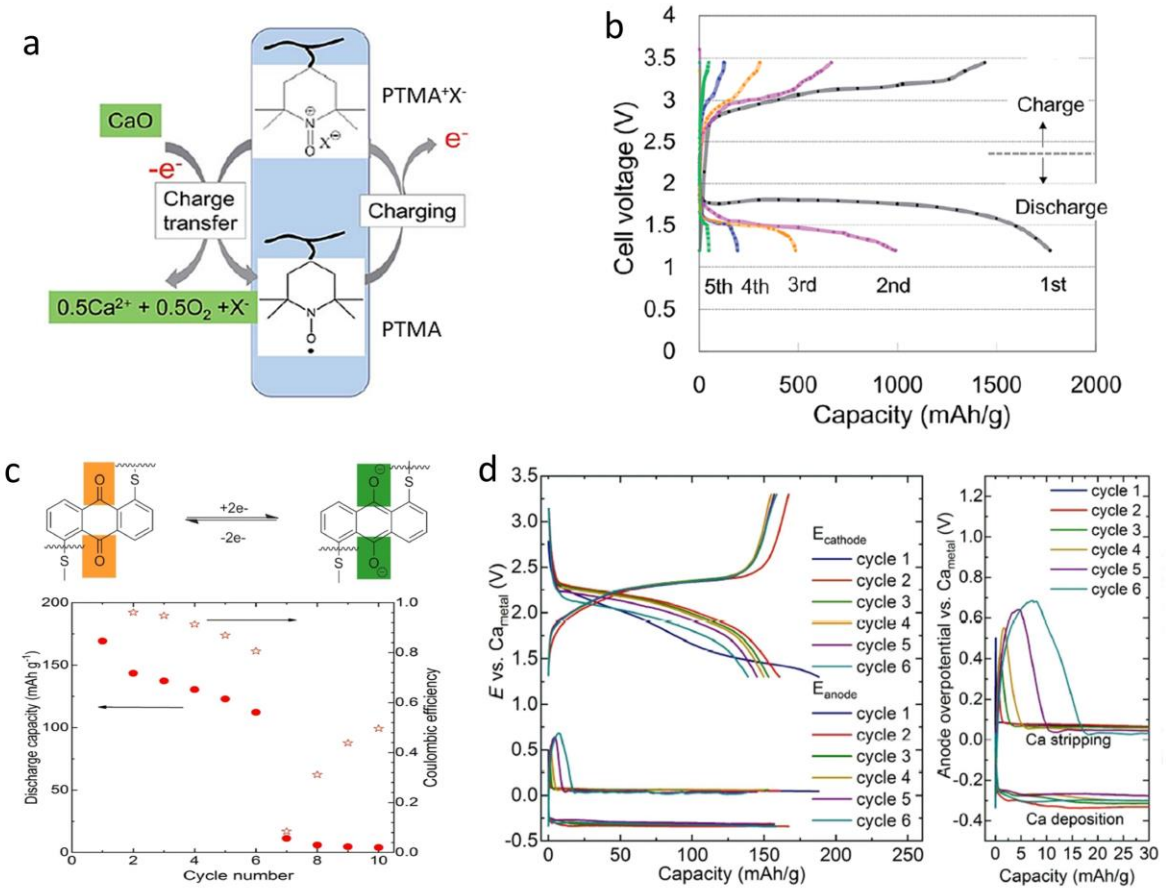

Figure 11 Electrochemical performance for Ca-O_2 and Ca-organic batteries. (a) Schematic illustration of the working processes and (b) discharge/charge voltage profiles of a Ca-O_2 battery using TEMPO as catalyst;[113] (c) electrochemical reaction of PAQS (up) and cyclic capacities of PAQS/CNT electrodes (down) in a two-electrode Ca-ion cell, (d) the potential curves of PAQS/CNT cathode (up) and the corresponding potential curves for Ca metal anode (down) of a three-electrode cell, the right in (d) showing the overpotential of Ca metal in the magnified voltage range.[116] Reprinted with permission (a, b),[113] copyright 2017 Royal Society of Chemistry, (c, d),[116] copyright 2020 WILEY-VCH GmbH, Weinheim.

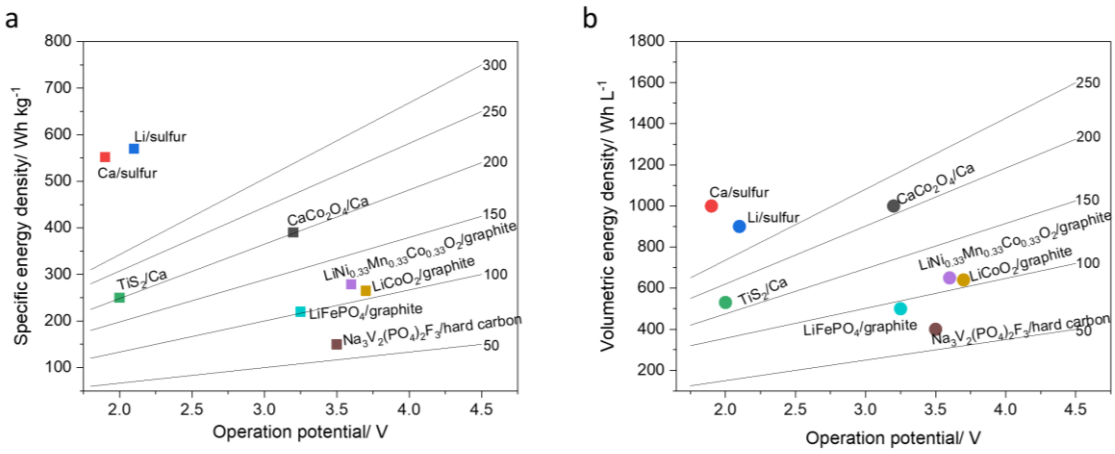

Figure 12 Comparison of CRBs with the state-of-the-art Li-ion battery, Na-ion battery and Li-S battery with respect to (a) specific and (b) volumetric energy densities. The straight lines are calculated energy densities of virtual Ca-ion batteries as a function of operation potential and capacities (at the right of each line). The data and calculations are derived from Monti *et al*.[117]

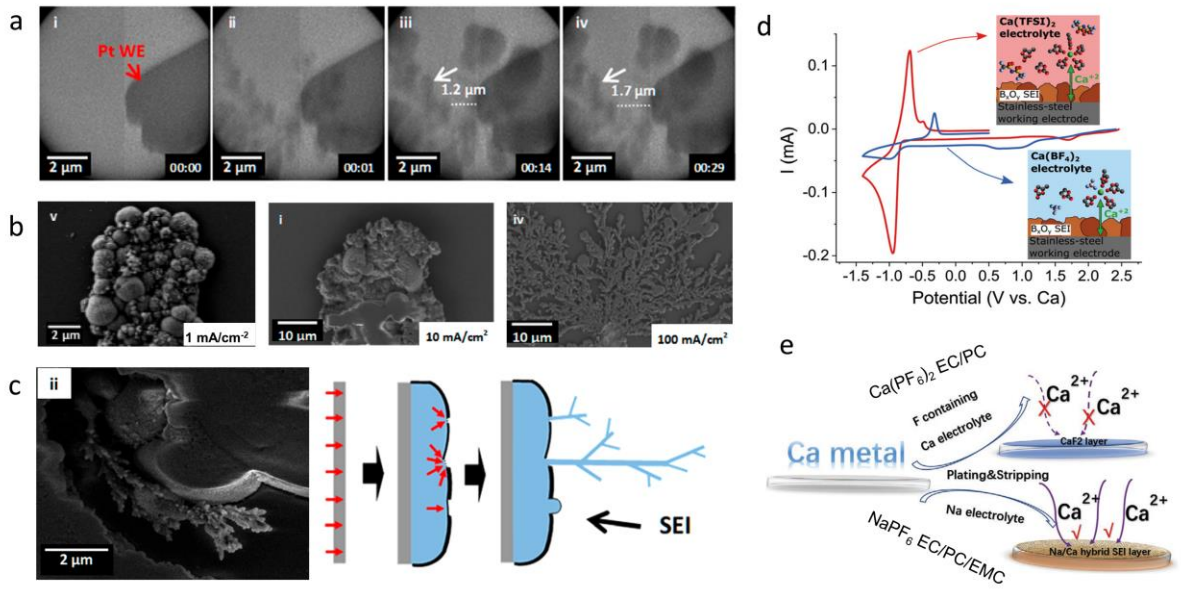

Figure 13 Mechanism analyses of Ca metal anode. (a) *In-situ* TEM observation of the formation and growth of Ca under galvanostatic discharge, (b) SEM images of Ca plating morphology for 1, 10 and 100 mA cm^{-2}, showing high current density induced Ca dendrite formation, (c) magnified SEM image showing Ca dendrite formed at Ca globular deposited at 10 mA cm^{-2} (left), indicating the influence of SEI inhomogeneity on dendrite formation (right);[119] (d) Ca plating behaviors regulated by the SEI layers formed in $Ca(BF_4)_2$ and $Ca(TFSI)_2$-based electrolytes;[121] (e) Ca deposition enabled by a Na/Ca hybrid SEI in $NaPF_6$ EC/PC/EMC electrolyte but forbidden by CaF_2 in $Ca(PF_6)_2$ EC/PC electrolyte in Ca metal electrodes.[124] Reprinted with permission (a-c),[119] copyright 2020 American Chemical Society, (d)[121] copyright 2020 Royal Chemical Society, (e)[124] 2020 WILEY-VCH GmbH, Weinheim.

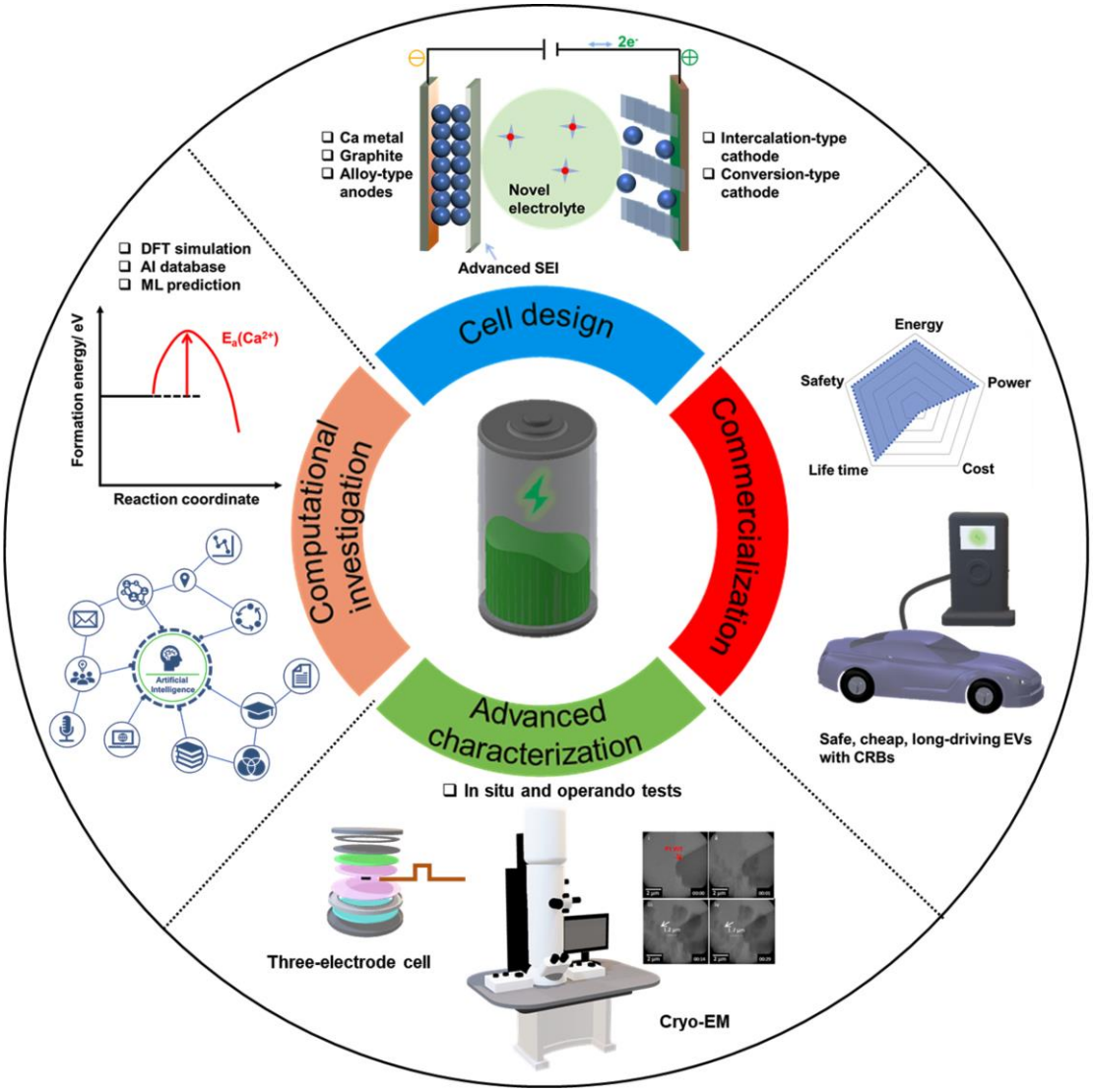

Figure 14 Perspectives of the development in CRBs. Computational and experimental characterizations function as powerful tools for mechanisms analysis of the working processes of CRBs, which in turn guides the design of high-performance electrode materials and cell configurations for future commercialization of CRBs.

Table 1 Summary of the reversible stripping and plating of Ca metal anodes in different nonaqueous electrolytes.

Electrolyte	Operation temperature / ℃	Anodic stability/ V	Ca plating substrate	Plating-stripping overpotential/ V at current/ mA cm^{-2}/cycle number	ICE/ %	SEI on Ca metal	Ref.
$Ca(BF_6)_2$/EC/PC, 0.45M	100	3.5 (Al) 2.5 (Pt)	Stainless steel	-0.52/-0.42/0.5/30	/	CaF_2	26
$Ca(BF_4)_2$/EC/PC, 1M	23	/	Cu	-1.2/0.25/0.55/10	~95	CaF_2	27
$Ca(BH_4)_2$/THF, 1.5M	25	~3.0 (Au)	Au	-0.25/0.25/1/50	94.8	CaH_2	28
$Ca(BH_4)_2$-$LiBH_4$ THF, 0.4/0.4M	25	/	Au	0.13/0.2/1/200	84.4	CaH_2, $CaCO_3$	30
$Ca[B(hfip)_4]_2$/DME, 0.25M	25	4.5 (Pt)	Pt	-0.3/0.22/80 mV s^{-1}/22	~50	CaF_2	31
$Ca[B(Ohfip)_4]_2$/DME, 0.5M	25	3.8 (Au) ~4.1 (Al)	Au	-0.25/0.25/0.2/20	~52	CaF_2	32
$Ca[B(hfip)_4]_2$/DGM, 0.25M	25	~4.1(GC) ~4.0 (Al) ~3.0 (Cu) ~5.0 (Pt)	GC, Al, Cu, Pt	-0.25/1.5/100 mV s^{-1} 0.1/1.4/100 mV s^{-1} 0.2/1.4/100mV s^{-1} 0.1/1.5/100 mV s^{-1}	85.5 61 76 82.1	/	35
$Ca(BH_4)_2$ ionic liquid, 1M	23	~3 (Cu)	Cu	-0.15/1.5/0.55/10	~56	CaS, CaF_2	40

Table 2 Summary of electrochemical performance of non-Ca metal anode materials for CRBs.

Anode	Electrolyte	Counter electrode	Operating voltage	Cyclic performance	Ref.
Graphite	0.5M $Ca(BH_4)_2$ DMAc	Ca	0.25-1.5 V *vs*. Ca^{2+}/Ca	~65 mAh g^{-1} after 50 cycles at 0.1A g^{-1}, ~70 mAh g^{-1} after 200 cycles at by rebuilding cells	50
Graphite	1M $Ca(TFSI)_2$ G_4	Activated carbon	-3-0 V *vs*. activated carbon	62 mAh g^{-1} after 10 cycles at 0.05A g^{-1}, 54 mAh g^{-1} after 1000 cycles at 0.5 A g^{-1}	51
Sn powder	0.2M $Ca(PF_6)_2$ EC/PC	$Na_{0.2}MnFe(CN)_6$	0-4 V Sn//$Na_{0.2}$MnFe-$(CN)_6$ full cell	~50 mAh g^{-1} after 35 cycles at 10 mA g^{-1}	54
Sn foil	1M $Ca(PF_6)_2$ EC/PC/DMC/EMC	Graphite	3-5 V Sn//graphite dual ion cell	530 mAh g^{-1} theoretical value	55

Table 3 Summary of electrochemical performance of cathode materials for CRBs.

Cathode	Electrolyte	Counter electrode	Operating voltage range	Cyclic performance	Ref.
$Mg_{0.25}V_2O_5•H_2O$	0.8M $Ca(TFSI)_2$ EC/PC/EMC/DMC	AC (activated carbon)	-2-1.5 V *vs*. AC	~90 mAh g^{-1} at 20 mA g^{-1} after 100 cycles, 70.2 mAh g^{-1} at 100 mA g^{-1} after 500 cycles	14
$NH_4V_4O_{10}$	$Ca(ClO_4)_2$ AN	Ag/$AgNO_3$	-0.3-1.0 V *vs*. Ag^+/Ag	150 mAh g^{-1} at 100 mA g^{-1} after 100 cycles, 61 mAh g^{-1} at 1 A g^{-1}	66
V_2O_5	1M $Ca(ClO_4)_2$ AN	Ag/$AgNO_3$	-1.5-0.5 V *vs*. Ag^+/Ag	~450 mAh g^{-1} for c-V_2O_5, ~500 mAh g^{-1} for a-V_2O_5 at 50 µA cm^{-2}	68
V_2O_5-PC	0.4M $Ca(ClO_4)_2$ PC	AC	-1.0-1.0 V *vs*. AC	~270 mAh g^{-1} at 7.58 mA g^{-1} at 70 ℃, ~300 mAh g^{-1} at 150 ℃	73
TiS_2	0.3M $Ca(TFSI)_2$ PC	Ag/AgCl	-1.75-0.75 V *vs*. Ag^+/Ag	~300 mAh g^{-1} at C/50 after 9 cycles	81
Ca_xMoO_3	0.1M $Ca(TFSI)_2$ AN	AC	0.9-2.9 V *vs*. Ca^{2+}/Ca	~80 mAh g^{-1} at 2 mA g^{-1} after 12 cycles	77
$Ca_{0.13}MoO_3·(H_2O)_{0.41}$	0.5M $Ca(ClO_4)_2$ AN	AC	-1.25-1 V *vs*. AC	85.3 mAh g^{-1} at 2C after 50 cycles	78
$CaCo_2O_4$	1M $Ca(ClO_4)_2$ AN	Ag/AgCl	-0.25-1.75 V *vs*. Ag^+/Ag	~80 mAh g^{-1} at 40 µA after 30 cycles	84
$CaMoO_3$	0.4 M $Ca(BF_4)_2$ EC/PC	Ca	0-4 V *vs*. Ca^{2+}/Ca	~200 mAh g^{-1} at C/200 at 70 ℃ PITT charge	24

Na_2FePO_4F	0.2M $Ca(PF_6)_2$ EC/PC	AC	-1.5-3V *vs*. AC	~60 mAh g^{-1} at 10 mA g^{-1} after 50 cycles	93
$Na_xMnFe(CN)_6$	0.2M $Ca(PF_6)_2$ EC/PC	AC	-1-3 V *vs*. AC	~70 mAh g^{-1} at 10 mA g^{-1} after 3 cycles	54
$NiFe(CN)_6$	0.2M $Ca(PF_6)_2$ EC/PC	AC	-1-3 V *vs*. AC	~20 mAh g^{-1} at 10 mA g^{-1} after 50 cycles	99
$K_2BaFe(CN)_6$	1M $Ca(ClO_4)_2$ AN+6 ml H_2O	Ag/AgCl	-0.6-1.1 V *vs*. Ag^+/Ag	~50 mAh g^{-1} at 12.5 mA g^{-1} after 30 cycles	100
S/CMK-3	0.5M $Ca(ClO_4)_2$ AN	Ca	0-3 V *vs.* Ca^{2+}/Ca	~600 mAh g^{-1} based on sulfur at C/3.5 discharge	108
S/C	0.2M $Ca(CF_3SO_3)_2$-$LiCF_3SO_3$TEGDME	Ca	0-3 V *vs*. Ca^{2+}/Ca	~300 mAh g^{-1} based on sulfur at C/10 after 20 cycles	109
S/C	0.5M $Ca[B(hfip)_4]_2$ DME	Ca	0.5-3.5V *vs*. Ca^{2+}/Ca	900 mAh g^{-1} based on sulfur at C/10 at 1st cycle and 200 mAh g^{-1} after 15 cycles	111
PAQS/CNT	0.3M $Ca[B(hfip)_4]_2$ DME	Ca	1.25-3.25 V *vs*. Ca^{2+}/Ca	~120 mAh g^{-1} at 0.5C after 6 cycles	116